Title: Loss of the transcription factor *NEUROD2* causes a spectrum of neurobehavioral phenotypes in mice and humans

*Karen Runge [1] *, Rémi Mathieu [1] *, Stéphane Bugeon [2] *, Sahra Lafi [1,2], Corinne Beurrier [2 &], Surajit Sahu [1&], Fabienne Schaller [1], Arthur Loubat [1], Leonard Herault [3], Stéphane Gaillard [4], Mélanie Cahuc [1], Emilie Pallesi-Pocachard [1], Aurélie Montheil [1], Andreas Bosio [5], Jill A Rosenfeld [6], Eva Hudson [7], Kristin Lindstrom [8], Saadet Mercimek-Andrews [9], Lauren Jeffries [10],* Arie van Haeringen *[11], Olivier Vanakker [12], Bruno Pichon [13], Audrey Van Hecke [14], Dina Amrom [14], Sebastien Küry [15], Candace Gamble [7], Alfonso Represa [1], Carlos Cardoso [1] *, Harold Cremer [2] * and Antoine de Chevigny [1,£]*

[1] INMED INSERM U1249, Aix-Marseille University, Marseille, France

[2] IBDM, Aix-Marseille University, CNRS, UMR 7288, Marseille, France

[3] TAGC INSERM U1090, Aix-Marseille University, Marseille, France

[4] Phenotype Expertise, 5 Boulevard du Maréchal Koenig, 13009 Marseille, France

[5] Miltenyi Biotec, Bergisch-Gladbach 51429, Germany.

[6] Baylor College of Medicine, Houston, Texas, USA

[7] Department of Pediatrics, University of Texas Health Medical School, Houston, TX 77030, USA

[8] Division of genetics and Metabolism, Phoenix Children's Hospital, Phoenix, Arizona, USA

[9] Genetics and Genome Biology Program, Research Institute, the Hospital for Sick Children, Toronto, Ontario, Canada

Division of Clinical and Metabolic Genetics, Department of Pediatrics, University of Toronto, Toronto, Ontario, Canada

Institute of Medical Sciences, University of Toronto, Toronto, Ontario, Canada

[10] Pediatric Genomics Discovery Program, Department of Pediatrics, Yale University School of Medicine, New Haven, Connecticut, USA

[11] Department of Clinical Genetics, Leiden University Medical Center, 2300 RC, Leiden, Netherlands

[12] Center for Medical Genetics, Department of Biomolecular Medicine, Ghent University and Ghent University Hospital, Ghent, Belgium

[13] Erasme Hospital, Route de Lennik 808, 1070 Brussels, Belgium

[14] Department of Neurology, Queen Fabiola Children's University Hospital, 15 JJ Crocq Avenue, 1200 Brussels, Belgium

Université Libre de Bruxelles (ULB), Brussels, Belgium

Neuropediatric Unit, Kannerklinik, Centre Hospitalier de Luxembourg, Luxembourg, Grand-Duchy of Luxembourg

[15] Centre Hospitalier Universitaire de Nantes, Service de Génétique Médicale, 9 quai Moncousu, 44093 Nantes, France

INSERM, CNRS, UNIV Nantes, l'institut du thorax, 44007 Nantes, France

[£] Author for correspondence:
Antoine de Chevigny, PhD
Research Associate
INMED INSERM U901
Campus de Luminy
13273 Marseille Cédex 09
antoine.de-chevigny@inserm.fr
+33 4 91 82 81 84

[*, &] equal contribution

Number of figures: 7
Number of Tables: 2
Supplementary figures: 5

Number of words for Abstract: 196
Number of words for Introduction: 685
Number of words for Discussion: 1565

Abstract:

The neuronal transcription factor NeuroD2 has recently been associated with early encephalopathic epilepsy [1] and genome-wide association studies (GWAS) have suggested that it might be a candidate for neuropsychiatric disorders [2]. We set out to understand the function of *NeuroD2* in cortex development and behavior and found that deleting this factor in mice results in altered migration, laminar positioning, structural synaptic maturation and physiology of cortical projection neurons (CPNs), as well as in differential expression of genes associated with neuronal excitability, synaptic transmission and neurodevelopmental disorders. These cellular and molecular defects were correlated with behavioral defects, namely locomotor hyperactivity, altered social interest and social memory, stereotypic behaviors and spontaneous seizures. Informed by these neurobehavioral features in mouse mutants, we identified individuals with *de novo* and familial heterozygous missense mutations in *NEUROD2* or copy number variations involving *NEUROD2*, who shared clinical features such as intellectual disability (ID) and autism spectrum disorder (ASD), with sometimes hyperactivity and epilepsy. In vitro functional analyses showed that *NEUROD2* missense mutations identified in a non-consanguineous family and a sporadic case were both pathogenic. Our study demonstrates that loss-of-function mutations in *NEUROD2* cause a spectrum of neurobehavioral phenotypes including ID and ASD.

Keywords: cortical pyramidal neuron, *NEUROD2* gene, synaptic maturation, human mutations, neurodevelopmental disorders

Introduction

Alterations in cellular development, synaptic transmission and intrinsic excitability of projection neurons in the neocortex [3,4] are prevalent theories of the pathophysiology of neurodevelopmental and neuropsychiatric disorders including ID, ASD and schizophrenia (SCZ) [5-7]. Despite a field of intense investigation, the transcription factors that regulate these processes in CPNs remain poorly understood. NeuroD2 belongs to the family of NeuroD basic helix-loop-helix transcription factors that regulate neuronal differentiation during development [8]. While cortical expression of its closest and first identified paralog NeuroD1 is turned off around birth [8], NeuroD2 cortical expression persists postnatally [9], indicating that it might be involved in processes other than early neuronal differentiation [8]. Indeed, few recent studies have suggested a possible link between NeuroD2 and synapse formation. First, *NeuroD2* mutant mice have a reduced density of synaptic markers in amygdala [10]. Second, Bonni and colleagues found that the degradation of NeuroD2 by the ubiquitin-proteasome system is necessary for the normal differentiation of presynaptic terminals in cultured cerebellar neurons [11]. Finally, a study from Ince-Dunn et al. showed that the electrophysiological maturation of the thalamo-cortical synapse is altered in the barrel cortex of *NeuroD2* deficient mice [12].

A possible involvement of *NEUROD2* in neuropsychiatric disorders has recently emerged. In a recent study two children with early infantile epilepsy were found to carry *de novo NEUROD2* variants, and functional analyses in tadpoles suggested that these variants were pathogenic [1]. Moreover, several lines of evidence suggest that *NEUROD2* might be associated with SCZ, ID and/or ASD. First, a GWAS has demonstrated an association between rare *NEUROD2* polymorphisms and SCZ [2]. Second, *NEUROD2* mRNA contains a high-confidence putative target site for the well-described SCZ-related microRNA miR-137 [13,14], according to miRNA prediction algorithms (TargetScan, miRanda). Third, the main transcriptional cofactor of NEUROD2 is the Pitt-Hopkins syndrome gene TCF4 that confers ID [15-18]. Fourth, copy number variations encompassing *NEUROD2* are associated with ID and/or ASD in the DECIPHER database (https://decipher.sanger.ac.uk/). Fifth, a machine learning based algorithm for the prediction of ASD-related genes ranked *NEUROD2* 98th among all human genes [19] – a better

rank than many confirmed ASD genes -, which suggests that *NEUROD2* is a gene in the genetic network associated with ASD. Together, these pieces of evidence support the hypothesis that *NEUROD2* might be associated with neuropsychiatric disorders in humans.

Besides hippocampus and amygdala, the cerebral cortex is the brain structure that is the most strongly associated with neuropsychiatric diseases [3,4]. However, current knowledge about the role of NeuroD2 in cortex is limited. *NeuroD2* deficient mice have a disorganized barrel cortex although production of layer 4 (L4) CPNs is normal [12]. Electrophysiologically, L2/3 CPNs show increased intrinsic excitability in somatosensory cortex [20]. In spite of this information, the impact of NeuroD2 deletion on cortical development has not been investigated.

Here we studied the development of the cerebral cortex in *NeuroD2* KO mice and analyzed mouse behaviors in relation with human neuropsychiatric disorders. We report an over-migration of CPN precursors that resulted in an altered CPN laminar positioning at P30. At this age, spine density and turnover were altered in L5 CPNs of the sensorimotor cortex. At the electrophysiological level, these neurons were too responsive to inhibitory inputs and showed increased excitability. At the molecular level, differentially expressed (DEX) genes in NeuroD2 null *vs* WT mice preferentially encoded voltage-gated ion channels and synaptic proteins, and the human orthologs of DEX genes were very strongly enriched in neuropsychiatric disorder associated genes. Finally, at the behavioral level, *NeuroD2* KO mice displayed lower sociability and social memory but unaltered interest and memory for objects; they also presented stereotypies, spontaneous epilepsy and hyperactivity. Informed by these neurobehavioral features in mouse mutants, we identified two individuals with relatively small heterozygous deletions encompassing *NEUROD2*, 3 individuals with *de novo* heterozygous missense mutations and 1 non consanguineous family (6/8 individuals affected) with a paternal inherited *NEUROD2* heterozygous missense mutation, who all shared similar clinical symptoms including ID and ASD, together with less frequent epilepsy or hyperactivity. Altogether, we provide experimental evidence for a causal relationship between NeuroD2 loss-of-function, functional defects in CPNs and a neurobehavioral syndrome that includes ID and ASD.

Material, Patients & Methods:

Animals

Mice (mus musculus) were group housed (2–5 mice/cage) with same-sex littermates on a 12 hour light-dark cycle with access to food and water ad libitum. NeuroD2 deficient mice were previously described [21,22]. Mice were bred and maintained on a mixed SVeV-129/C57BL/6J background. Experimenters were always blinded to genotypes during data acquisition and analysis. Animal experiments were carried out in accordance with European Communities Council Directives and approved by French ethical committees (Comité d'Ethique pour l'expérimentation animale no. 14; permission number: 62-12112012). Male mice were used for behavioral experiments, while mice of either sex were used for all other experiments.

Immunostainings

Mice were perfused transcardially with ice-cold 4% paraformaldehyde (in PBS). Brains were removed and post-fixed overnight at 4°C with the same fixative. Coronal sections were cut at 50 μm thickness using a cryostat (Leica) or a sliding microtome (Microm).

Immunofluorescence experiments were performed as described before [23]. Briefly, free-floating sections were blocked and permeabilized for one hour in a "blocking solution" composed of 10% Normal Goat Serum, 0.2% Triton X-100 (Sigma) in PBS. Primary antibodies, diluted in blocking solution and added overnight at 4°C, were as follows: rabbit anti-NeuroD2 (1:500, Abcam, #ab104430), rabbit anti-Tbr1 (1:1000, Abcam, #31940), rat anti-Ctip2 (1:100, Abcam, #ab18465), rabbit anti-Cux1 (1:200, Santa Cruz Biotechnology, #sc13024), mouse anti-Rorβ (1:200, Perseus Proteomics, #PP-N7927-00), chicken anti-GFP (1:500, Aves, #GFP-1010). Corresponding fluorescently labeled secondary antibodies (AlexaFluor, Invitrogen) were added for 2 hours in blocking solution. Hoechst was added in PBS for 10 minutes, and sections were mounted on microscope slides that were coversliped using Mowiol solution (Sigma).

In Utero Electroporation

Timed pregnant NeuroD2 heterozygous females fertilized by heterozygous males (E13.5) were anesthetized with isoflurane (7.5% for induction and 3.5% for surgery). The uterine horns were exposed. A volume of 1–2 µL of DNA plasmid (pCAGGS-RFP, 0.5 µg/µL) combined with Fast Green (2 mg/ mL, Sigma) was injected into the lateral ventricle of each embryo with a pulled glass capillary and a microinjector (Picospritzer II, General Valve Corporation, Fairfield, NJ, USA). Electroporation was then conducted by discharging a 4000 µF capacitor charged to 50 V with a BTX ECM 830 electroporator (BTX Harvard Apparatus, Holliston, MA, USA). Five electric pulses (5 ms duration) were delivered at 950 ms intervals using electrodes. Embryos were collected 5 days post-electroporation (at E18.5), and 80 µm coronal slices cut using a sliding microtome (Microm). Electroporated cortices were imaged with an Apotome microscope (Zeiss). Quantification of red fluorescent protein (RFP)-expressing cell distribution was performed on cortical column crop images (bottom: above VZ/SVZ, below IZ; top: brain surface) using a custom-made algorithm on Fiji. We counted the proportion of total RFP-positive cells that were found in each of 20 bins of equal size along the width of the cortical column.

Laminar positioning, radial migration and layer thickness measurements

Images used to analyze the lamination of CPN subtypes at P30 and of *in utero* electroporated neurons at E18.5 were acquired using an apotome microscope (Zeiss) with a 10x objective. Typically, three stacks with 1 µm z-steps centered in the mid depth of each slice were imaged and a maximum intensity projection was generated. Cortical columns were cropped in stereotyped positions of the somatosensory cortex. For P30 mice lower and upper limits of the cropped images were the dorsal border of corpus callosum and the L1-L2 boundary, respectively. For E18.5 pups, crop limits were SVZ-IZ boundary and pial surface, respectively. Blind manual counting of marker-positive cells was made in 20 bins using Image J.

For radial cell quantification of PNs, 5 slices per animal were selected in defined levels of the rostro-caudal axis. For each slice, a cortical column was cropped in the somatosensory cortex by using PhotoShop software. Each cortical column was divided into 20 Bins of equal size

spanning the cortical thickness. Cells were quantified in each bin, and bin-distribution was defined as the percentage of cells in each bin relative to the total number of cells.

For layer thickness measurement, the same slices were used. For each slice, the layer thickness was measured at the left edge, the right edge and the middle of the cortical column and the mean of these 3 values was calculated. Limits of the layer thickness were defined by only taking into account strong fluorescent cells. Layer thickness of each slice was then calculated relatively to the whole cortex thickness.

For radial cell quantification of electroporated cells, slices were selected at 3 defined levels of the rostro-caudal axis. The same method than the one for radial cell quantification of PNs was applied as previously detailed.

All counts were manually performed by an investigator who was blinded to genotype.

Dendritic reconstructions and length measurement

For 3D dendritic reconstructions, Thy1-GFP expressing PNs were imaged as 3D stacks using a Zeiss LSM 800 confocal microscope with a ×20 objective and a 0.5 µm z-step. Neurons were reconstructed three-dimensionally using Imaris software. Digital reconstructions were analyzed with Imaris to measure the total dendritic length.

Spine density measurements

For spine analyses, images were acquired as 3D stacks with lateral and z-axis resolution of 100 nm and 380 nm using a Zeiss LSM 800 confocal microscope, with an oil-immersed 63X objective. For the quantitative and morphological analyses of dendritic tree spines, basal and apical dendrites were imaged separately using a ×63 oil objective, roughly placing the soma at the center of the image. During the same imaging session, randomly selected dendrites were imaged by using the same objective and adding a 3.4 numerical zoom. For basal dendritic spines, dendrites 5–100 µm distal to the first bifurcation away from the soma were imaged. For apical dendritic spines, dendrites within 5-100 µm of the pial dendritic ending were imaged. Spine quantifications were performed on z-stacks using NeuronStudio [24]. Imaging and

quantifications were all performed blindly to experimental groups.

In vivo trans-cranial two-photon imaging for spine turnover measurements

Four-week-old NeuroD2/Thy1-GFP mice were ketamine/xylazine anesthetized. The skin over the skull was incised, and the skull was cleaned to ensure adhesion, using activator (10% citric acid). An aluminum bar was then glued and cemented using dental cement (Super-Bond C&B) on the skull, caudally to Bregma, keeping the skull parallel to the bar. The animal was then placed in a stereotaxic frame, attached to the metal bar, and the primary motor cortex was marked (coordinates: +1.0 AP; +2.0 ML). Using a scalpel blade, the skull was gently thinned until less than 20 µm thickness, avoiding any bleeding, breaking or extensive drying of the skull. Dendritic segments that were bright and visible were located and marked on a low magnification z-stack and then imaged at high resolution (axial resolution: 0.21 µm; step size: 0.79 µm). After imaging the skin over the skull was stitched and animals received a subcutaneous injection of Carprofen (5 mg/kg) and Buprenorphine (0.3 mg/kg). Three days after the first imaging session, animals were anesthetized and the skin covering the skull was re-opened. Next, the skull was cleaned and new images of each dendritic segment were taken. New and eliminated spines were then determined blindly, comparing images at day 0 and at day 3 on ImageJ, on single z-planes.

Image Analyses

All cells (lamination and radial migration experiments), dendrites and spines analyzed were located in the M1 and S1 cortex. Image analyses were always performed with the scientists blinded to the experimental conditions (we used a custom-made R algorithm to blind all data). Manual quantifications of CPN lamination, dendrite and spine parameters by 2 independent qualified scientists gave similar results.

Quantitative reverse transcription polymerase chain reaction (qRT-PCR). Total RNAs were extracted from whole cortices (for developmental expression of NeuroD2 in Fig. S1, n =

3-4 brains per stage in each condition) or from the pooled motor and somatosensory areas (for confirmation of RNAseq data in Fig. 5a, n=3 samples) using TRIZOL reagent according to manufacturer's instructions (Life Technology). cDNA was synthesized from 1 µg of total RNA using Quantitect Reverse Transcription Kit and according to manufacturer protocol (Qiagen). RT-PCRs were then carried out using SYBR-Green chemistry (Roche Diagnostics) and Roche amplification technology (Light Cycler 480). PCR primers (Table below) were designed for 12 mouse genes, and for 3 control genes, *Ptgs2* (Prostaglandin-Endoperoxide Synthase 2), Rpl13a (Ribosomal protein L13a) and *Hprt1* (Hypoxanthine Phosphoribosyltransferase 1) for normalization. All primer pairs were optimized to ensure specific amplification of the PCR product and the absence of any primer dimer. Quantitative PCR standard curves were set up for all. Values of fold change represent averages from duplicate measurements for each sample.

Gene	Forward	Reverse
NeuroD2	AAGCCAGTGTCTCTTCGTGG	GCCTTGGTCATCTTGCGTTT
Scn4b	GAACCGAGGCAATACTCAGG	ACGACAGGTACATGGGAAGC
Kcnk4	CACTCACTGGCCTGGACAA	GAGCTCCTGGGGAGCAGT
Scn8a	CAAGCTGGAGAATGGAGGCA	TAAGAGGGGAGGGAGGCTGT
Kcnh1	GGTGAGAATGTTCACAAGCACT	ACTGGGGAAGGATGTCTGAA
Scn1a	GGTTTGAGACCTTCATTGTGTTC	TTTTGATCGTCTTTCGCTGA
Kcnq5	TACAGGAGCAGCACCGCCAG	CCTTGTTCTTTCTTGGTAGGGC
Cacna1c	CCCTTCTTGTGCTCTTCG TC	TTGTGCATCTTTCCCATG AA
Grin2b	TGCTGTAGCTGTCTTTGTCTTTG	CTTTGCCGATGGTGAAAGAT
Htr2a	CTGCTGGGTTTCCTTGTCAT	GTAAATCCAGACGGCACAGAG
Cdh8	GTGACCCTGATATCACTTCCAGT	TCTTCCCATCATCTGCATTG
Ppia1	QT00247709	QT00247709
Rpl13a	CCCTCCACCCTATGACAAGA	GCCCCAGGTAAGCAAACTT
HPRT	QT00166768	QT00166768

Electrophysiological recordings. Coronal slices (250 µm) from 21 to 30 days-old mice were cut with a VT 1000S vibratome (Leica) in ice-cold high-choline artificial cerebro-spinal fluid (ACSF) containing (in mM): 130 choline, 2.5 KCl, 1.25 NaH_2PO_4, 7 $MgCl_2$, 0.5 $CaCl_2$, 25 $NaHCO_3$ and 7 glucose at 4°C. Slices were then maintained at room temperature in oxygenated ACSF containing (in mM): 126 NaCl, 2.5 KCl, 1.2 NaH_2PO_4, 1.2 $MgCl_2$, 2.4 $CaCl_2$, 25 $NaHCO_3$ and 11 glucose, to which 250 µM kynurenic acid and 1 mM sodium pyruvate were added. Slices were then transferred one at a time to a submersion recording chamber and

were perfused continuously with ACSF warmed to 33°C at a rate of 2.5-3 ml/min. All solutions were equilibrated with 95% O_2/ 5% CO_2. Neurons were visualized on an upright microscope (Nikon Eclipse FN1) equipped with DIC optic and filter set to visualize EYFP using a x40 water-immersion objective. Recordings were interleaved in control and *NeuroD2* KO mice.

Miniature excitatory and inhibitory postsynaptic currents (mEPSCs and mIPSCs, respectively) were recorded in whole-cell configurations in voltage-clamp mode in oxygenated ACSF containing tetrodotoxin (TTX, 1 μM). Patch-clamp electrodes (4-6 MΩ) were filled with an intracellular solution of the following composition (in mM): 120 $CsMeSO_4$, 12.3 CsCl, 0.1 $CaCl_2$, 1 EGTA, 10 HEPES, 4 MgATP, 0.3 NaGTP, pH adjusted to 7.25 with CsOH and osmolarity adjusted to 270-280 mOsm/L. Cells were kept at -60 mV, the reversal potential for GABAergic events, or -4 mV, the reversal potential for glutamatergic events, for the recordings of mEPSCs and mIPSCs, respectively. In some experiments, picrotoxin (50 μM) and 6-cyano-7-nitroquinoxaline-2,3-dione (CNQX, 10 μM) were applied at the end of the experiment to verify that the currents were indeed GABAergic and glutamatergic, respectively. Access resistance was monitored throughout the experiments with a 5-mV negative step and was found to be constant.

To measure intrinsic properties, we used current-clamp recordings. Glass electrodes (6–9 MΩ) were filled with an internal solution containing the following (mM): 130 $KMeSO_4$, 5 KCl, 10 4-(2-hydroxyethyl)-1-piperazineethanesulfonic acid, 2.5 MgATP, 0.3 NaGTP, 0.2 ethyleneglycoltetraacetic acid, 10 phosphocreatine, and 0.3-0.5% biocytin, pH = 7.21. Access resistance ranged between 15- 22 MΩ, and the results were discarded if the access resistance changed by >20%. TTX, was obtained from Abcam, CNQX from Tocris and picrotoxin and kynurenic acid from Sigma.

Data were collected with a MultiClamp 700B amplifier (Molecular Devices), filtered at 2kHz, digitized (10kHz) with a Digidata 1440A (Molecular Devices) to a personal computer, and acquired using Clampex 10.1 software (PClamp, Axon Instruments, Molecular Devices). Data were analyzed and plotted in clampfit (Molecular Devices, v 10.2). Miniature currents were analyzed with Mini Analysis (Synaptosoft, version 6.0.7).

Retrograde tracing

P28 mice under xylazine/ketamine anesthesia received stereotaxic injections of 0.3 µl of cholera toxin subunit B (CT-B, 1 mg/ml; Thermo Fisher Scientific) conjugated with Alexa Fluor 647 in the striatum (AP: +1 mm; ML: +1.8 mm; DV: −2.9 mm from dura) and conjugated with Alexa Fluor 488 in the thalamus (AP: −1.3 mm; ML: +1.15 mm; DV: −3.5 mm from dura) using Bregma coordinates. This allowed retrograde labeling of, respectively, L5 PNs (striatal injection) and L6 PNs (thalamic injection). Another group of animals were injected with Alexa Fluor 488 CT-B in motor cortex (AP: 0.6 mm; ML: 1.3 mm; DV: 0.7 mm). Ten days after injection, animals were trans-cardially perfused with 4% paraformaldehyde, their brains processed and cut 50 µm thick using a sliding microtome (Microm).

RNA Isolation and library preparation

Tissue from motor plus somatosensory cortex of P28 mice was rapidly micro-dissected and frozen at -80˚C (n=3 independent experiments for WT and KO samples, 1 to 4 mice per sample). Total RNA was purified using spin columns of the RNeasy Mini Kit (Qiagen) according to manufacturer's protocol. Library preparation was made with the TruSeq mRNA-seq Stranded v2 Kit sample preparation (Illumina) according to manufacturer's instructions. One µg total RNA was used for poly(A)-selection and Elution-Fragmentation incubation time was 8 min to obtain 120-210 bp fragments. Each library was barcoded using TruSeq Single Index (Illumina). After library preparation, Agencourt AMPure XP (Beckman Coulter, Inc.) was performed for 200 to 400 bp libraries size-selection (282 nt average final library size). Each library was examined on the Bioanalyzer with High Sensitivity DNA chip (Agilent), quantified on Qubit with Qubit® dsDNA HS Assay Kit (Life Technologies), diluted to 4 nM and then pulled together at equimolar ratio.

Illumina NextSeq-500 sequencing

Sequencing was performed by the TGML Facility (INSERM U1090) using PolyA mRNA isolation, directional RNA-seq library preparation and the Illumina NextSeq 500 sequencer.

The denaturation was performed with 5 µl of pooled libraries (4 nM) and 5 min incubation with 5 µl of fresh NaOH (0.2N) and then addition of 5 µL of fresh Tris-HCl (200 mM - pH 7), according to manufacturer's instructions. The dilution of 20 pM pooled libraries was performed with HT1 to a 1.2 pM final concentration. PhiX library as a 1% spike-in for use as a sequencing control was denatured and diluted, and 1.2 µl was added to denature and dilute pooled libraries before loading. Finally, libraries were sequenced on a high-output flow cell (400M clusters) using the NextSeq® 500/550 High Output v2 150 cycles kit (Illumina), in paired-end 75/ 75nt mode, according to manufacturer's instructions.

RNA-seq data primary analysis

467 548 934 clusters were generated for 71 Gbp sequenced with 75 % >= Q30. Reads were first trimmed with sickle v1.33 (Joshin et al., 2011) (RRID:SCR_006800) with parameters –l 25 –q 20 and then aligned to mm10 using STAR v2.5.3a (Dobin et al., 2013) to produce BAM alignment files. Multi-mapped reads and reads with more than 0.08 mismatches per pair relative to read length were discarded. Transcriptome assembly were performed with Cufflinks v2.2.1 (Trapnell C. et al 2010) (RRID:SCR_014597) using the relative UCSC mm10 GTF file. For each sample Cufflinks assembles the RNA-Seq reads into individual transcripts, inferring the splicing structure of the genes and classified them as known or novel. The output GTF files from each of the Cufflinks analysis and the GTF annotation file were sent to Cuffmerge v2.2.1 (Trapnell C. et al 2010) (RRID:SCR_014597) to amalgamate them into a single unified transcript catalog.

Isoform expression analysis from RNAseq data

Transcript expression in fragments per kilobase of exon per million reads mapped (FPKM) were estimated and normalized using Cuffdiff v2.2.1 (Trapnell C. et al 2010) (RRID:SCR_014597) with default parameters from Cuffmerge GTF file result and alignment files. The R package CummeRbund v2.16 (Trapnell C et all 2012) (RRID:SCR_014568) was used for data exploration and figure generation of some isoforms of interest.

Differential gene expression analysis

Gene counts were calculated with featureCounts v1.4.6-p4 (Liao Y et al., 2014) (RRID:SCR_012919) from a GTF containing known UCSC mm10 genes as well as the novel genes detected by Cufflinks (Cufflinks class code "u") and alignment files. The R package DESeq2 v1.14.1 (Love MI et al., 2014) (RRID:SCR_000154) was then used to normalize counts and detect the differentially expressed genes (FDR < 0.05). Batch effect between replicates was added in the design formula of DESeqDataSetFromMatrix function to model it in the regression step and subtract it in the differential expression test.

Data access

The RNA-Seq data discussed in this publication have been deposited in NCBI's Gene Expression Omnibus and are accessible through GEO Series accession number GSE110491 (https://www.ncbi.nlm.nih.gov/geo/query/acc.cgi?acc=GSE110491).

Gene ontology

Gene ontology enrichment was performed using all of the expressed genes as background. We used DAVID (RRID:SCR_003033) with high stringency parameters [25], and ClueGo (Cytoscape) [26] with a similar approach. DAVID adjusted p-values were used for further evaluation.

RNA-Seq statistics

We assumed that the samples were normally distributed. *P*-values for overlaps were calculated with binomial test using a custom-made R script. *P*-values were subsequently adjusted for multiple comparisons using Benjamini-Hochberg FDR procedure. Two-way permutation test of 1000 was adapted to validate the overlaps. We randomized the differentially expressed gene sets by randomly selecting same number of genes from RNA-seq expressed genes and subsequently calculating the overlap P-values. Moreover, we adapted a permutation test to evaluate the detected differentially expressed genes, randomizing 1000 times the RNA-seq

data and recalculating the differentially expressed genes. Analysis for RNA-seq was performed using custom made R scripts implementing functions and adapting statistical designs comprised in the libraries used. The heatmap for gene expression was performed from the gene overlap file using scripts written on R.

Behavior.

All behavioral tests were done with age-matched male 8 to 14 weeks old littermates. They were performed according to the European Union and national recommendations for animal experimentation. The experimenter was blind to the genotypes during all analyses.

Open field test. The test was performed in a 40 x 40 cm square arena with an indirect illumination of 100 lux. Mouse movements were video-tracked using Smart 3.0 software (Panlab, Harvard apparatus) for one hour. Total distance traveled, time in center (exclusion of a 5 cm border arena), resting time and mean velocity were measured. The open-field arena was cleaned and wiped with H20 and 70% ethanol between each mouse. Data shown are means +/- s.e.m. and were analyzed using one way ANOVA or Kruskall-Wallis ANOVA when required. (WT : n=16 ; HET : n=15 ; KO : n=15).

Stereotypic behavior*.* During the first 10 minutes of the open-field test, the number of rearing and circling were measured manually. Both on-wall and off-wall rearing were counted. An on-wall rearing event was counted when both front-paws were apposed on the wall. An off-wall rearing event was counted when both front paws had left the floor. A complete 360-degree turn of nose angle with respect to the mouse body center was counted as one circling event. Data shown are means +/- s.e.m. and were analyzed using Kruskall-Wallis ANOVA. (WT : n=16 ; HET : n=15 ; KO : n=15).

Three-chamber test. The test was performed as described previously [27] with modifications. The three-chamber apparatus consisted of a Plexiglas box (60 x 40 cm, each chamber being

20 x 40 cm) with removable floor and partitions dividing the box into three chambers with 5-cm large openings between chambers. Test mice were housed individually the day before the test. The task was carried out in five trials of 5 min each. After each trial, the mouse was returned to his home cage for 15 min. The three-chambers apparatus was cleaned and wiped with 70% ethanol between each trial.

In the first trial, a test mouse was placed in the center of the three-chamber unit, where two empty wire cages were located in the left and right chambers to habituate the test mouse. The mouse was allowed to freely explore each chamber. The mouse was video-tracked for 5 minutes with Smart 3.0 software. In the second trial, an 8-weeks old C57Bl/6J mouse (M1) was placed randomly in one of the two wire cages to avoid any place preference. The second wire cage remained empty (E). The test mouse was placed in the center, and allowed to freely explore the chamber for 5 min. In the following two trials, the same mouse M1 was again placed in one of the wire cages, and the test mouse was placed in the center and allowed to explore each chamber. The goal of these 2 trials was to familiarize the test mouse with M1. In the last 5-min session, a new 8-weeks old C57Bl/6J mouse (M2) was placed in the second wire cage. Thus, the test mouse had the choice between a now familiar mouse (M1) and a new, stranger mouse (M2). Time spent in each chamber and time spent within a 5-cm square proximal to each wire cage with the nose towards the cage (that we called investigation time) were measured. All data presented are means +/- s.e.m. and analyzed using two-way ANOVA with Bonferroni's post hoc analysis. (WT : n=14 ; HET : n=15 ; KO : n=13).

New object recognition test. The arena used for the novel object recognition test was the same used for the open-field test. The arena was cleaned and wiped with 70% ethanol between each mouse. For habituation, the tested mouse was placed in the arena and allowed to explore for 10 min. Following habituation, two identical objects (50 ml orange corning tube) were placed in opposite corners of the arena, 10 cm from the sidewalls. The tested mouse was placed in the center of the arena, and allowed to explore the arena for 10 min. After 24 h, one object was replaced with another novel object, which was of similar size but differed in shape

and color with the previous object (white and blue LEGO® bricks). The test mouse was placed in the center, and allowed to explore the arena and the two objects (a new and an "old" familiar object) for 10 min. The movement of the mice was video-tracked with Smart 3.0 software. Time in each proximal area (nose located in a 2 cm area around the object) was measured. All data shown are means +/- s.e.m. and analyzed using Student's two-tailed, paired t-test or Wilcoxon Signed Rank Test when required. (WT : n=16; HET : n=15 ; KO : n=15).

Consent and human ethics approval

All subjects or their legal representatives gave written informed consent for the study. Except for family 3 and 4 for which the study was approved by the institutional review Board (IRB) at Yale University, studies of other families in the present work used unlinked anonymized data and were performed in accordance with the Declaration of Helsinki protocols and approved by the Dutch, USA and Belgian ethics committees. The clinical cytogenetic sample consisted of patients referred to the Netherlands, USA, and Belgium from regional pediatricians, other health specialists and/or genetics centers.

Patients

The study includes 9 patients from 6 unrelated families in the Netherlands, USA, Mexico, Canada and Belgium. These patients were identified in centers where High-throughput Sequencing (whole-exome sequencing, whole-genome sequencing) is being used to identify, or accurately characterize, genomic variants in individuals with developmental brain abnormalities, mental retardation, epilepsy and ASD. Clinical information, brain MRI, and blood were obtained after informed consent. DNA from subjects was extracted from peripheral blood lymphocytes by standard extraction procedures.

In vitro *NEUROD2* pathogenicity test

P19 cells culture and transfection were performed with modification from Farah et al., 2000 [28]. P19 mouse carcinoma cells were cultured in MEMα with 7.5% bovine serum and 2.5% fetal

bovine serum (HyClone) containing Glutamax and essential amino acids (Gibco), and maintained subconfluent prior to transfection. For lipofectamine 2000 (Invitrogen) transfections, cells were plated on glass coverslips in 24-well dishes at a concentration of 50,000 cells per well and transfected 24 hours later following manufacturer's instructions. Three plasmids were co-transfected in each condition: pCAG-Cre, pCALNL-DsRed and pCALNL-*NEUROD2, NEUROD2* being either the WT form or any of 5 variants (see Fig. 5c). Cells were fixed 3 days post-transfection, immunostained for βIII-tubulin (BioLegend BLE801201, 1:1000), counterstained with Hoechst solution (Molecular Probes) and mounted. For each condition we analyzed 2-3 independent experiments with 3 coverslips each.

Statistics

All statistical tests are described in the figure legends. All values represent the averages of independent experiments ± SEM. Statistical significance for comparisons with one variable was determined by Student's t-test using two-tailed distribution for two normally distributed groups, and by Mann-Whitney test when distributions were not normal. Significance of multiple groups was determined by one-way, two-way, or two-way repeated measure ANOVA followed by either Bonferroni's post hoc test as indicated in figure legends. RNA-seq statistics are described above. Differences were considered significant when $P < 0.05$. All statistical analyses were performed with Prism 6 software (Graphpad).

Results

Cortical expression of NeuroD2 mRNA and protein across development

We first examined the cortical expression of NeuroD2 throughout development. Quantitative real time PCR from whole cortices of embryonic and postnatal stages showed that NeuroD2 mRNA increased from E14.5 to reach an expression peak at E18.5, and remained at lower albeit constant levels postnatally (Fig. 1a). In situ hybridizations from ALLEN BRAIN ATLAS (http://www.brain-map.org/) revealed that NeuroD2 mRNA is expressed in the cortical plate and hippocampus starting from E13.5 onwards (Fig. 1b and Supplementary Fig. 1a). In the postnatal cortex, NeuroD2 mRNA was maintained after birth, and observed in L2 to L6 at all ages examined.

At the protein level, NeuroD2 was also detected embryonically in the intermediate zone where migration occurs and in the cortical plate (Fig. 1c and Supplementary Fig. 1b for at E16.5), confirming results of a previous study [29]. NeuroD2 expression was maintained postnatally in cortical L2 to L6 (Fig. 1c and Supplementary Fig. 1c-d). NeuroD2 protein co-localized with Ctip2 in L5 pyramidal tract CPNs (Supplementary Fig. 1e,f) and was also found in CPNs of other layers (not shown) at all ages examined (P3, P30 and P90). Strikingly, NeuroD2 protein was never detected in Gad67-GFP^{+} inhibitory neurons (Supplementary Fig. 1f,g for P30, but P3 and P90 were also investigated), nor in non-neuronal cortical cells (not shown). In sum, NeuroD2 was found in migrating in post-migratory CPNs of L2 to L6.

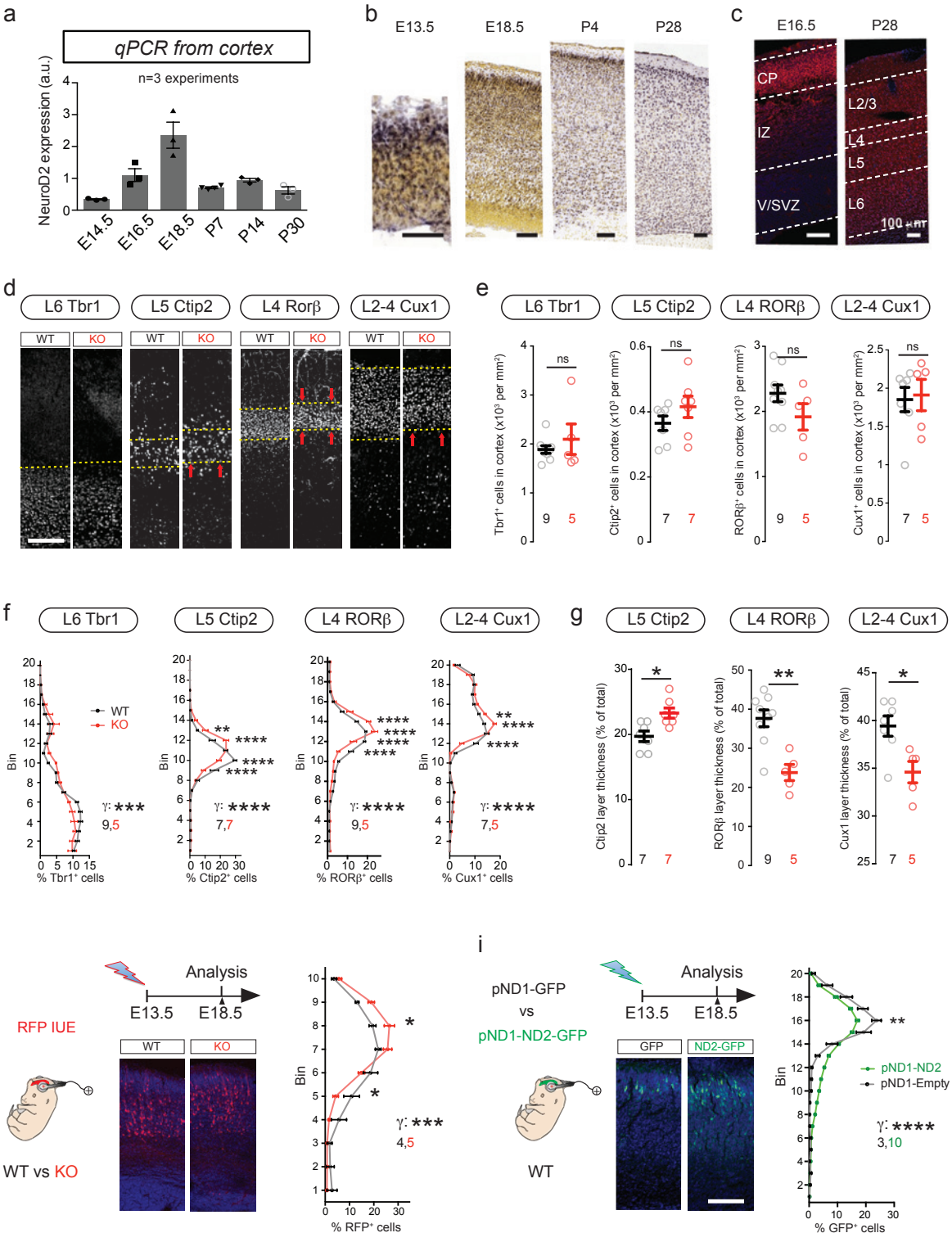

Figure 1: Altered laminar position and excess radial migration of CPNs in *NeuroD2* null mice. (a-c) Cortical expression of NeuroD2 across development. (a) qPCR shows permanent cortical expression of *NeuroD2* mRNA with a peak expression at E18.5. (b) In situ hybridizations from Allen Brain Atlas confirm permanent *NeuroD2* mRNA expression across cortical layers and ages (S1 shown). (c) NeuroD2 protein expression at E18.5 and P28 in the S1 cortex.

(d-g) Number and laminar distribution of PNs from different cortical layers in NeuroD2 null mice. Tbr1$^+$ cortico-thalamic and Ctip2$^+$ subcortical PN layers extended superficially, at the expense of RORβ$^+$ and Cux1$^+$ superficial PNs that were compressed below the pial surface. Total number of Tbr1, Ctip2, RORβ and Cux1$^+$ cells per cortical column were unaltered, indicating unchanged production of PNs.

(h-i) NeuroD2 expression cell-autonomously regulates radial migration of L5 PNs during. (h) RFP-electroporated PNs settled more superficially in *NeuroD2* null mice compared with WT littermates. (i) Post-mitotic overexpression of NeuroD2 in PNs of WT mice induced a reduced migration of electroporated cells.

Data are represented as means ± SEM. Statistical significance was evaluated by Student t-test or Mann-Whitney test depending on normality of samples [(d)-(g)] or by two-way ANOVA followed by Bonferroni's post-hoc test [(d)-(i)] (*P < 0.05, **P < 0.01, ***P < 0.001, ****P < 0.0001).

Altered relative size of cortical layers in NeuroD2-deficient cortex

We analyzed the gross anatomy of the *NeuroD2* KO cortex at P30, an age when cortical neurons should have stopped migrating and maturing. The corpus callosum of NeuroD2-null mice had a slightly reduced width (Supplementary Fig. 2a-b), but global cortical anatomy appeared otherwise normal, as indicated by the normal aspect and thickness of the cortical wall at sensorymotor levels (Supplementary Fig. 2c-d).

The specialization of CPN subtypes is largely determined by their axonal outputs [30-32]. Thus, we asked if axonal targeting specificities of CPN subtypes were altered in absence of NeuroD2. We injected the retrograde tracer cholera toxin beta (CTB) at each of the three main axonal target regions of motor and somatosensory cortices: the ventrolateral thalamus targeted by L6 cortico-thalamic PNs, the striatum preferentially targeted by a subset of L5 CPNs, and L2-5 of M1 targeted by contralateral L2-5 callosal CPNs [33,34]. Thalamic, striatal and M1 injections retrogradely labeled CPN somata in L6, L5 and contralateral L2-5, respectively (Supplementary Fig. 2e-f), like in WT littermates. Labeling major forebrain axonal tracts using L1 immunostaining confirmed normal organization of major axonal tracts (Supplementary Fig. 2a-b). Thus, axonal targeting specificities of CPN subtypes were normal in *NeuroD2* KO mice.

Then, we quantified the amount and laminar distribution of CPN subtypes in S1 and M1 using immunostainings for major regulatory TFs of selected cortical layers. We used Tbr1 for L6, Ctip2 for L5 pyramidal tract, RORβ for L4 and Cux1 for L2-4 PNs [35]. Each CPN subtype was found in normal quantities in cortical columns (Fig. 1d-g), suggesting unaltered proliferation and apoptosis of CPN precursors during development. This was to be expected given that NeuroD2 is not expressed in VZ progenitors. Moreover, the inside-out patterning was normal since Tbr1, Ctip2, RORβ and Cux1 were successively expressed from deep to superficial layers as expected. However, Tbr1 and Ctip2-expressing deep layers extended superficially towards the pial surface in *NeuroD2* KO mice (Fig. 1d,e). This extension of L5-6 induced an enlargement of L5 towards the brain surface at the expense of RORβ and Cux1-expressing superficial L2-4 (Fig. 1f,g), so that overall cortical width was unaltered (Supplementary Fig. 2d).

Longer migration of layer 5 PN in the NeuroD2-deficient cortex

The increased *vs* decreased surfaces occupied by L5-6 *vs* L2-4 in NeuroD2-null mice might result from altered radial migration or from abnormal neuronal morphogenesis and/or maturation at post-migratory stages. To discriminate between these two hypotheses, we analyzed the radial migration of CPN precursors using *in utero* electroporation. A fluorescent reporter plasmid was electroporated at E13.5 when cortical progenitors generate L5 CPNs, and embryos were sacrificed at E18.5, around the end of radial migration [36]. Precise positioning analyses using quantification in 20 bins showed that in KO mice a higher fraction of electroporated CPNs were located in superficial layers at E18.5, indicating over-migration (Fig. 1h). Conversely, overexpressing NeuroD2 only in post-mitotic CPNs of WT mice using the *NeuroD1* promoter increased the fraction of electroporated cells in deep layers at E18.5 compared to a control group, indicating that NeuroD2 cell autonomously shortens radial migration (Fig. 1i). Taken together, these data indicate that NeuroD2 cell autonomously controls the laminar positioning of CPNs by limiting the distance of their radial migration during

corticogenesis. This explains that in null mice CPNs over-migrate, which results in altered relative thicknesses of deep and superficial layers at P30.

Altered synaptic density and turnover in NeuroD2 null mice

Our expression data indicate that *NeuroD2* is expressed in maturing CPNs confirming the hypothesis that this transcription factor can be playing a regulatory role on synaptogenesis [37]. We gained experimental access to the fine morphology of L5 CPN dendrites and spines - the post-synaptic elements of excitatory synapses - by using the Thy1-GFP mouse, line M [38,39]. At P30, total lengths of basal and apical dendrites of L5 CPNs in M1 were not significantly altered in NeuroD2 null mice (Fig. 2a,b). In contrast, spine density in those dendrites was reduced in both basal and apical compartments, with L1-located apical dendrites being more strongly affected (Fig. 2c-h). Surprisingly however, spine densities in both compartments caught up on normal levels by 4 months of age (Fig. 2e,h). To gain insight into the temporal dynamics of spine formation, we compared spine densities at 1 vs 4 months. In WT mice spine density dropped down between 1 and 4 months in basal and apical dendrites. In *NeuroD2* KO mice however, in this time window dendritic spine density declined exclusively in basal but not in apical dendrites (Fig. 2h).

These data suggest that spine turnover in L5 CPN apical tufts might be abnormal from P30 in NeuroD2 mutant mice. We used 2-photon live microscopy to measure this parameter in M1. We imaged the same dendritic segments at P30 and P33, an age when total spine density was reduced in *NeuroD2* KO mice (Fig. 2i). Spine gain and loss compensated for each other in WT mice (Fig. 2j,k) over the 3-day observation period. In contrast, gained spines outnumbered lost spines in *NeuroD2* KO mice (Fig. 2j,k), resulting in a net spine gain over 3 days (Fig. 2l). In sum, spine density was still increasing at P30 in *NeuroD2* KO mice, in contrast to WT mice where it had reached a plateau. This indicates that the development of excitatory synapses is delayed in L5 CPN apical tufts of *NeuroD2* KO mice.

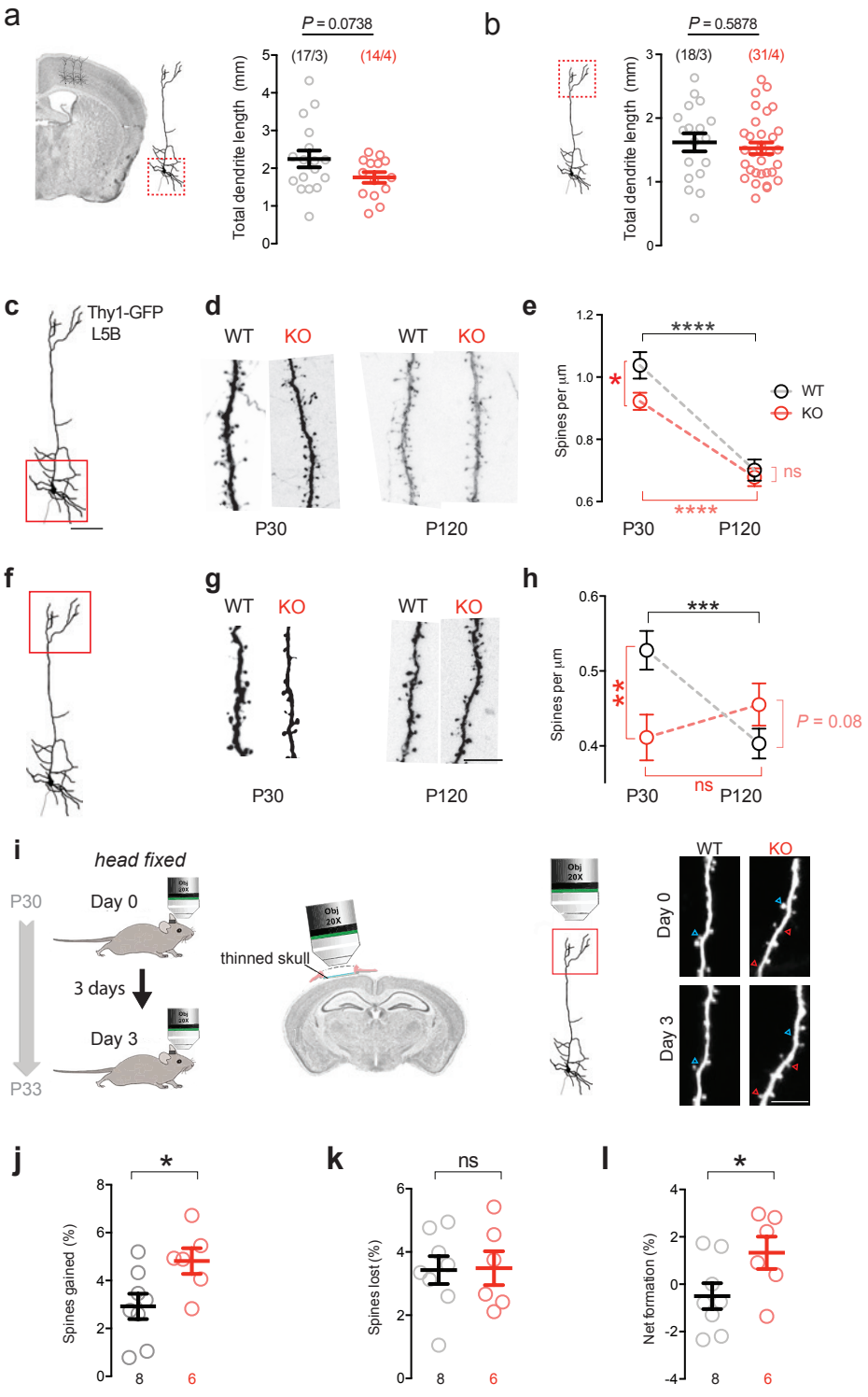

Figure 2: Synaptic deficits in basal and apical dendrites of CPNs in *NeuroD2* KO mice.

(a,b) Total lengths of basal (a) and apical (b) dendrites of L5 CPNs were not significantly altered.

(c-e) Age-dependent spine density defects in basal dendrites. (d) Representative photomicrographs at P30 and P120 (scale bar 10 µm), (e) Subtle reduction in spine density at P30 but no difference P120. Note the significant spine density reduction between P30 and

P120 in both genotypes. N= 16 dendritic segments from 3 WT mice and 33 segments from 7 KO mice at 1 month, 33 segments from 3 WT and 27 segments from 3 KO mice at 4 months. (f-h) Age-dependent spine density defects in apical tuft dendrites. (g) Photomicrographs at P30 and P120 (scale bar 10 μm). (h) Quantification showing significant reduction of spine density at P30 but not P120.

(i-l) Increased acute spine gain and net spine formation in apical tuft dendrites at P30. (i) Experimental paradigm and representative images. Blue arrowheads depict lost spines while red arrowheads depict gained spines over 3 days. (j) Spine gain, (k) spine loss and (l) spine net formation. Data are represented as means ± SEM. Statistical analyses were performed using two-tailed t-tests or Mann-Whitney test depending on the normality of samples. **P* < 0.05, ***P* < 0.01, ****P* < 0.001, *****P* < 0.0001.

Electrophysiological characterization of L5 PNs in *NeuroD2* KO mice

The lamination and dendritic spine phenotypes at P30 prompted us to analyze electrophysiological properties of L5 CPNs at this age. The frequency of somatic miniature excitatory post-synaptic currents (mEPSCs) was unaltered (Fig. 3a-c), which was expectable since spine loss was most prominent in apical tuft branches that are far from somatic electrophysiological recordings. The amplitude of mEPSCs was also unaltered (Fig. 3d). When measuring miniature inhibitory post-synaptic current (mIPSCs) we found no change in frequency (Fig. 3e,f) but an increased amplitude in *NeuroD2* KO mice (Fig. 3g). Because L2/3 CPNs receive reduced mEPSC and mIPSC frequencies but normal amplitudes [20], we conclude that defects in inputs received by L5 PNs differ from defects in inputs received by L2/3 CPNs in *NeuroD2* KO mice.

Next, we measured intrinsic physiological properties in L5 CPNs. First, resting membrane potential as well as action potential threshold and amplitude were normal in *NeuroD2* KO mice (Fig. 3h-j). However, input membrane resistance was increased (Fig. 3k) and capacitance was decreased (Fig. 3l). Interestingly, L5 CPNs in *NeuroD2* KO mice fired significantly more action potentials than in WT littermates in response to depolarizing current injections (Fig. 3m,n), demonstrating increased intrinsic excitability. This increased excitability was neither due to

variations in action potential after-hyperpolarization (Fig. 3o) - which contrasts with L2/3 CPNs in NeuroD2 deficient mutant [20] - nor to alterations in resting membrane potential or action potential threshold and amplitude (Fig. 3h-j). Finally, we measured hyperpolarization-activated cation (HCN) Ih currents since they influence intrinsic neuronal excitability [40] and are critical integrators of synaptic integration selectively in L5 CPNs [41,42]. Compared with WT mice, L5 CPNs in *NeuroD2* KO mice exhibited a significantly increased Ih current density (Fig. 3p,q), suggesting that *NeuroD2* deficiency alters expression or function of HCN channels. Since increased Ih current usually down-tunes intrinsic neuronal excitability [40], this phenotype might represent a compensatory mechanism that counter-balances NeuroD2-induced neuronal hyper excitability.

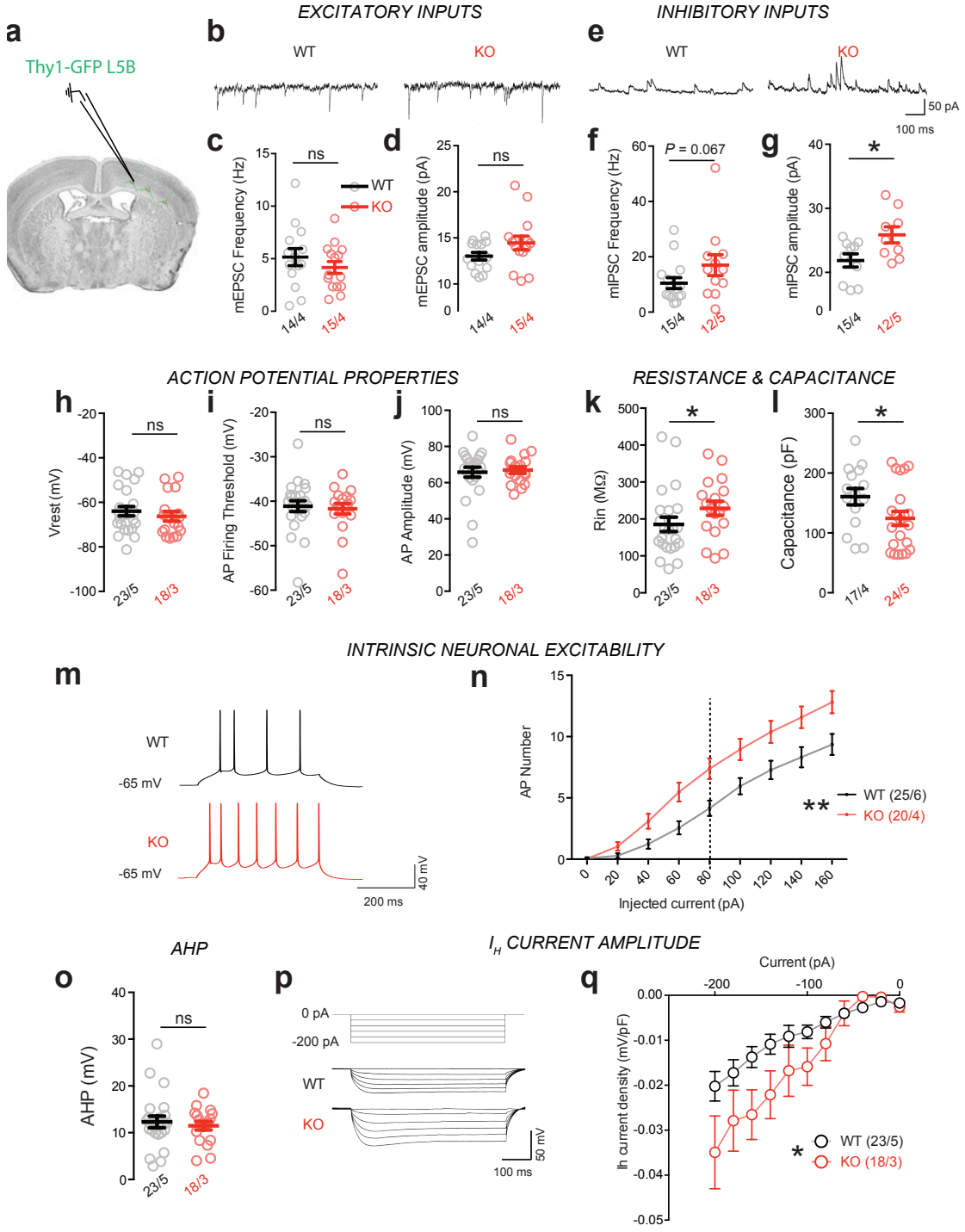

Figure 3: Electrophysiological characterization of L5 CPNs in *NeuroD2* null mice.

(a-g) Miniature post-synaptic currents. Representative traces (b), frequency (c) and amplitude (d) of mEPSCs. Example traces (e), frequency (f) and amplitude (g) of mIPSCs. Amplitude of mIPSC was increased (g).

(h-j) Action potential properties, including Vrest (h), AP firing threshold (i) and AP amplitude (j). (k,l) Membrane resistance (k) and capacitance (l).

(m-n) Intrinsic excitability. Representative firing responses to +80 pA current steps in a WT (top) and a KO (down) cell. (n) *NeuroD2* KO neurons reached action potential (AP) firing threshold earlier than WT neurons and exhibited a steeper input-output relationship, as assessed by the number of APs elicited by increasing current injections (from +20 to +160 pA, 20-pA increments) during current-clamp recordings.
(o) After-hyperpolarization (AHP) was normal in L5 PNs of *NeuroD2* KO mice.
(p,q) *NeuroD2* KO L5 PNs exhibited increased Ih-current amplitudes compared with WT PNs (current/voltage relation of Ih currents). (p) shows experimental protocol and representative traces, (q) shows summary graph of the voltage-current relation.
Data are means ± SEM. Number of cells/ animals analyzed are shown in graphs in parentheses. Statistical significance was evaluated by unpaired t-test for samples with normal distributions [bar graphs in (b), (c), and (f)], by Mann-Whitney test for non-normal samples [bar graph in (e)], and by two-way repeated measure ANOVA [(n) and (q)] followed by Bonferroni's post hoc test. $*P < 0.05$; $**P < 0.01$.

Differential gene expression in the juvenile *NeuroD2* KO cortex

Since NeuroD2 is a nuclear transcription factor, we sought to identify differentially expressed (DEX) genes in *NeuroD2* KO mice, again at P30. We micro-dissected the motor and somatosensory areas from WT *vs* KO mice and subjected the tissues to RNA-seq [3]. Comparative analyses of RNA-seq identified 264 DEX genes (Fig. 4a; Supplementary File 1), including 185 genes with decreased expression and 79 genes with increased expression in KO mice (representing 70% *vs* 30% of the total DEX genes, respectively). Using quantitative PCR (qPCR), we validated some DEX genes in *NeuroD2* KO mice (Fig. 4b). Some DEX genes were specific to selected cortical layers and the proportion of layer-specific DEX genes was similar in L2/3, L5 and L6 (Fig. 4c,d), in agreement with the idea that NeuroD2 impacts CPNs from all layers.

Gene ontology (GO) analysis with DAVID [25] (Fig. 4e and Table 1) and ClueGO [26] (Supplementary Fig. 3) softwares revealed that DEX genes were most significantly enriched for voltage-gated ion channel activity, followed by cell projection morphogenesis and chemical synaptic transmission. DEX voltage-gated ion channels included the sodium channels Scn1a,

Scn4b and Scn8a, the potassium channels Kcnh1, Kcnq5, Kcnj6, Kcna5, Kcnv1, Kcnk4 and Kcnma1, and the calcium channels Cacna1c and Cacna2d2 (Fig. 4f), many of which are associated with neuropsychiatric syndromes (blue in Fig. 4f).

To further characterize DEX genes in *NeuroD2* KO mice, we compared our gene list with lists of ASD-associated genes [43] (SFARI database, 859 genes), FMRP-associated [44] (842 genes), ID-associated genes [45-48], SCZ-associated genes ([49] and OMIM, 196 genes) and synaptome-associated genes [50] (SynaptomeDB, 1876 genes) and generated a heatmap of expression levels (Fig. 4g). Strikingly, among the 264 DEX genes, 15% were associated with the synaptome, 12.5% with ASD, 14% with FMRP and 3.7% with SCZ (Fig. 4h). These proportions are much higher than what a random sampling would produce (Fig. 4i, and Supplementary File 2 for binomial test; hypergeometric test gave comparable significance). ASD/SCZ genes included the Dravet syndrome gene Scn1a and the Timothy syndrome gene Cacna1c that are both voltage-gated ion channels, but also Grin2b, Htr2a, Pcdh9 and many others (Fig. 5). Among synaptome associated DEX genes, 4 were pre-synaptic and 36 were post-synaptic [50] (Fig. 5 and Supplementary File 3).

In summary, a genetic network controlling neuronal activity and synaptic development that involves numerous known ASD and SCZ factors is regulated by NeuroD2 in the mouse P30 M1/S1 neocortex.

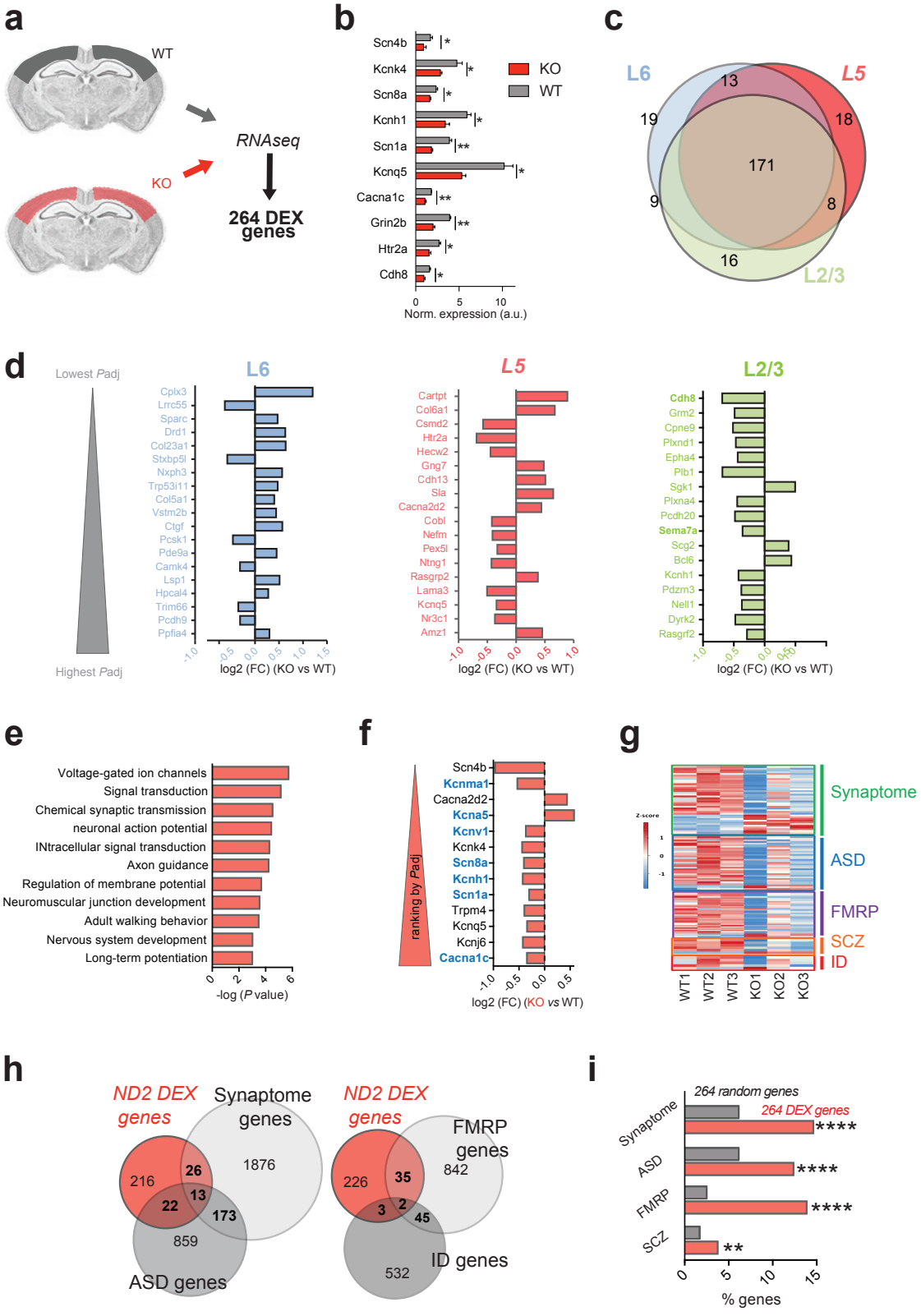

Figure 4: RNA-seq analysis of differentially expressed genes in motor/somatosensory cortex of P30 *NeuroD2* KO mice.

(a) Schematic of the experiment. (b) Validation of RNA-seq data by qPCR for several ion channel/ neuropsychiatric-related genes. N=3 experiments per genotype. (c) Venn diagram of DEX genes specific to L2/3, L5 and L6 (171 DEX genes are generic to all layers, some are common between 2 layers and others specific to a single layer). (d) Fold change expression (FC; log2 scale) of DEX genes belonging to specific layers, ranked according to adjusted P value (lowest Padj on top). (e) Results of gene set enrichment analysis using the DAVID knowledgebase. (f) Fold change expression (FC; log2 scale) of DEX genes belonging to the voltage-dependent ion channel family, ranked according to Padj (lowest on top). Genes associated with neuropsychiatric recurrent syndromes are depicted in blue. (g-i) Association of DEX genes with neuropsychiatric diseases. (g) Heatmap for synaptic and disease gene sets among DEX genes (red, higher expression; blue, lower expression). (h) Venn diagrams identifying overlaps between DEX genes and synaptic/disease gene sets. Number of genes for each gene set is indicated. (i) Graphical representation of % [DEX genes] (orange) vs % [same number of randomly selected genes] (grey) belonging to gene sets of interest. Statistical significance was evaluated by two-tailed Student t test [(b)] or binomial test [(i)] (*P < 0.05; **P < 0.01; ****P < 0.0001).

Table 1: Gene ontology of *NeuroD2* DEX genes in M1/S1 cortex with DAVID (https://david.ncifcrf.gov/).

	Term	Count	*P* Value	Benjamini	FDR
GLOBAL	Voltage-gated ion channel activity	13	1.91E-06	0.002	0.003
GLOBAL	Signal transduction	30	7.34E-06	0.005	0.012
GLOBAL	Chemical synaptic transmission	11	3.06E-05	0.013	0.050
GLOBAL	Neuronal action potential	6	3.71E-05	0.012	0.061
GLOBAL	Intracellular signal transduction	18	5.25E-05	0.014	0.086
GLOBAL	Axon guidance	11	5.99E-05	0.013	0.098
GLOBAL	Regulation of membrane potential	8	2.13E-04	0.039	0.347
GLOBAL	Neuromuscular junction development	6	2.85E-04	0.045	0.464
GLOBAL	Adult walking behavior	6	3.29E-04	0.046	0.536
GLOBAL	Nervous system development	15	9.69E-04	0.118	1.570
GLOBAL	Long-term synaptic potentiation	6	9.99E-04	0.111	1.618
DOWN	Voltage-gated ion channel activity	11	4.27E-06	0.004	0.007
DOWN	Axon guidance	10	1.75E-05	0.008	0.027
DOWN	Neuronal action potential	5	1.40E-04	0.042	0.218
DOWN	Regulation of membrane potential	7	1.91E-04	0.043	0.298
DOWN	Ion transport	15	2.68E-04	0.048	0.419
DOWN	Nervous system development	13	3.19E-04	0.048	0.498
DOWN	Chemical synaptic transmission	8	4.53E-04	0.058	0.705
DOWN	Signal transduction	20	5.17E-04	0.058	0.805
UP	Regulation of cell growth	4	0.002	0.701	2.977
UP	Insulin secretion	3	0.006	0.851	9.085
UP	Signal transduction	10	0.010	0.858	13.619
UP	Cell adhesion	7	0.012	0.824	15.969
UP	Positive regulation of stress fiber assembly	3	0.016	0.848	20.979

Table 1 Footnote: GLOBAL: all differentially expressed genes. DOWN: down-regulated genes. UP: up-regulated genes. FDR: False Discovery Rate.

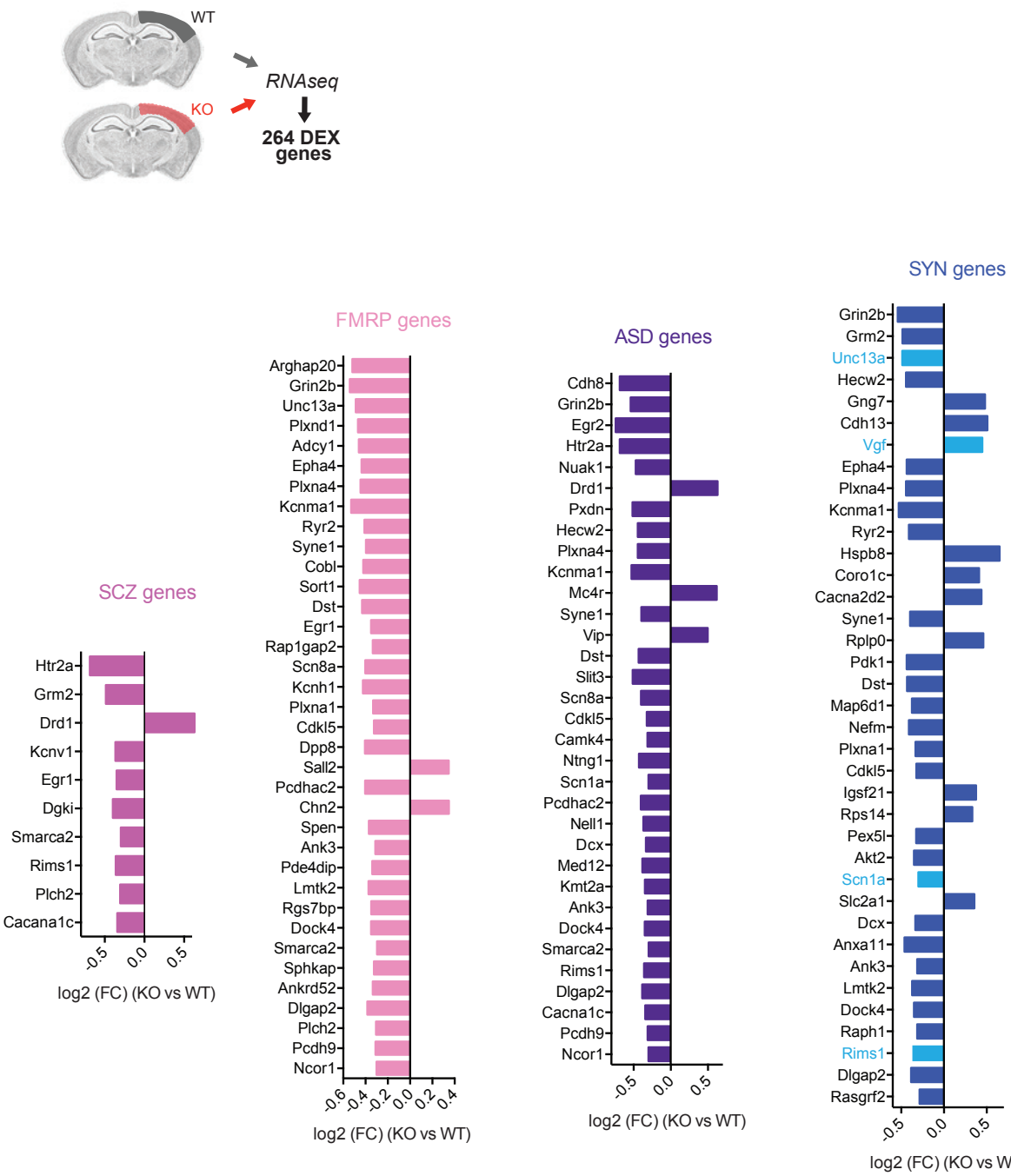

Figure 5: *NeuroD2* KO DEX genes associated with neuropsychiatric disorders. Fold change expression (FC; log2 scale) of DEX genes belonging to specific gene sets, ranked according to adjusted *P* value (lowest *P*adj on top). In the graph representing synaptome genes (SYN), presynaptic genes are depicted in light blue while postsynaptic genes are in dark blue.

Behavioral deficits in adult *NeuroD2* KO and HET mice

Since many ASD and SCZ-related genes were dysregulated in *NeuroD2* KO mice, we examined whether loss of NeuroD2 might produce neuropsychiatric disorder-like behaviors in

adults. We also analyzed heterozygous (HET) mice as they are more likely to reflect putative human *NEUROD2* loss-of-function mutations.

In the novel object recognition test, KO and HET mice showed normal interest and memory for objects since they spent 65-70% of their investigation time exploring a novel *vs* a familiar object, like WT littermates (Fig. 6e-g). This suggests that working memory for objects is not strongly dependent on NeuroD2.

In contrast, *NeuroD2* KO mice exhibited abnormal social interest and social memory, as demonstrated in the three-chamber test. First, unlike WT littermates, null mice showed no preference for the mouse-containing quadrant (Fig. 4h-j) or chamber (Supplementary Fig. 4a), indicating altered sociability. Mice with HET *NeuroD2* deletion behaved similar to WT in this task, however (Fig. 47j). Thus, KO but not HET mice showed reduced social interaction in the 3-chamber test.

In the social memory/interest test, WT mice showed strong preference for investigating the novel mouse, as expected. In contrast, *NeuroD2* KO, but also HET mice, did not show any preference for the novel mouse (Fig. 4k-m, Supplementary Fig. 4b). Thus, social memory/interest was impaired in both KO and HET mice.

Next, we analyzed stereotypies that constitute another core feature of ASD. Because WT, HET and KO mice displayed almost no grooming behaviors owing to their genetic background, we quantified two other types of ASD-related stereotypic behaviors, namely rearing and circling [51,52]. As previously described [53], HET mice displayed increased circling (Fig. 4n). Instead, NeuroD2 null mice showed increased rearing both at and outside the walls of the cage (Fig. 4n).

Epilepsy is a well-described comorbidity of ID [54], ASD [55] and SCZ [56]. One third of *NeuroD2* KO mice displayed spontaneous epileptic seizures observed at the behavioral level on videos (Fig. 4o and Supplementary Videos 1 and 2), which were lethal for 3 out of 5 KO mice. One HET mouse had a crisis, while in contrast no WT mice showed behavioral seizure activity. The proportion of epileptic seizures among *NeuroD2* KO and HET mice is likely an underestimate since mice were not monitored continuously.

Hyperactivity is another comorbid symptom of neuropsychiatric syndromes including ID, ASD and SCZ [57-60]. *NeuroD2* KO mice were hyperactive in the open field (Fig. 4p, Supplementary Fig. 4c). They travelled significantly more than WT and HET littermates, while HET mice displayed only subtle hyper-locomotion compared to WTs (Fig. 4p). KO mice displayed higher displacement velocities and shorter resting periods (Fig. 4p), confirming locomotor hyperactivity.

Finally, we measured conflict anxiety, which requires functional integrity of the cerebral cortex [61] and can be altered in ASD [62] and SCZ [63]. The open field arena presents a conflict between innate drives to explore a novel environment and safety. Under brightly lit conditions, the center of the open field is aversive and potentially risk-laden, whereas exploration of the periphery provides a safer choice. We found that HET and KO mice explored the center portion of the environment (as measured by the time of exploratory activity) more than their intact WT littermates did (Supplementary Fig. 4d).

In summary, *NeuroD2* KO mice exhibited behavioral defects that are reminiscent of the symptoms (altered social interest and memory, stereotypies) and comorbidities (epilepsy, hyperactivity, reduced conflict anxiety) of ASD and SCZ in humans. NeuroD2 HET mice had similar but milder phenotypes, indicating that NeuroD2 is a haploinsufficient gene.

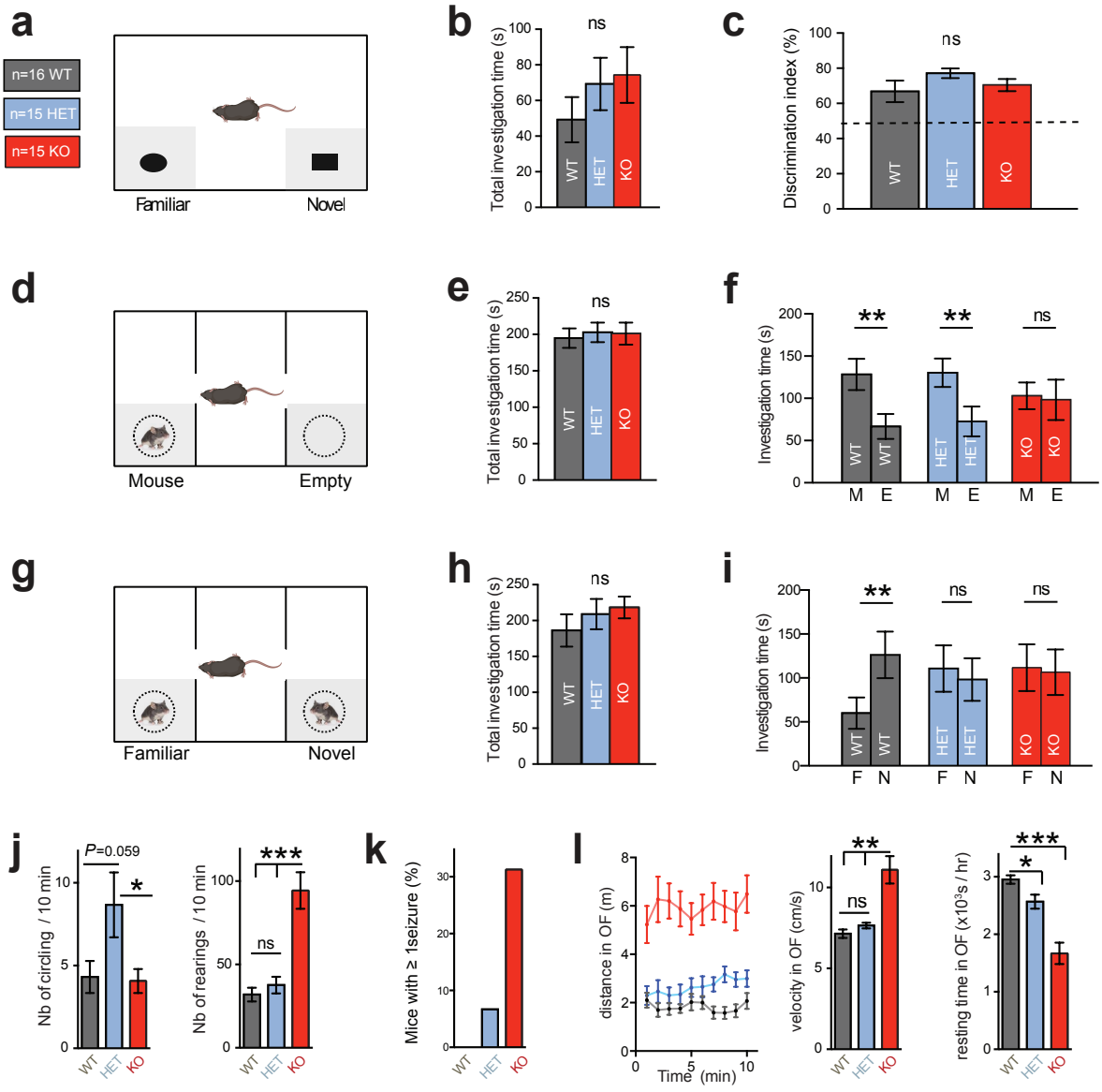

Figure 6: Behavioral hallmarks of neuropsychiatric disorders in NeuroD2 mutant mice

(a-c) In the novel object recognition test (a), *NeuroD2* KO and HET mice displayed unaltered total investigation time (b) and discrimination index between the familiar and the novel object (c). (d-f) During social interaction in the three-chamber test (d), all genotypes displayed similar total social investigation time (e). However, while WT and HET mice spent around twice more time investigating the mouse than the empty quadrant, *NeuroD2* KO mice spent equivalent times investigating mouse and empty quadrants (f). (g-i) Social memory/ interest test. When a familiar and a novel mouse were placed in each quadrant (g), all genotypes spent similar times having social interactions (h), but only WT mice spent significantly more time investigating the novel mouse, indicating altered social memory in HET and KO mice (i). (j) Circling (left graph) and rearing (right graph) behaviors in the 3 genotypes. (k) Spontaneous seizures were observed in a third of *NeuroD2* KO mice and in one HET mouse during the behavioral

experiments, but never in WT littermates. (l) Hyperactivity in *NeuroD2* KO mice. Left graph depicts the distance traveled in 1 minute-intervals during 10 minutes in the open field. Middle graph shows velocity during motion and right graph shows resting time, both during a 1-hour recording. N= 16 WT, 15 HET and 15 KO mice aged 8-14 weeks depending on the test. Data are means ± SEM. Statistical significance was evaluated by one-way ANOVA [(f), (g), (i), (l), (n) and (p)] or two-way ANOVA followed by Bonferroni's post hoc test [(j) and (m)] (n.s., not significant; **P* < 0.05; ***P* < 0.01; ****P* < 0.001).

NEUROD2 mutations associated with neurodevelopmental disorders in humans

Our studies showed that NeuroD2 has critical roles in cortical development that affect behavior. Guided by this knowledge we aimed at identifying patients with similar symptoms and mutations in *NEUROD2*. It is also worth noting that loss-of-function mutations in *NEUROD2* are predicted to be highly intolerable by the Genome Aggregation Database (gnomAD) with a probability of loss-of-function intolerance (pLI) = 0.94 (version 2.1.1). Through collaborative efforts, we had access to two individuals with relatively small 17q12.3-q21 deletions (1.57 Mb and 0.79 Mb) encompassing the *NEUROD2* gene *(*families 1 and 2 in Fig. 7b; Supplementary Fig. 5 and Supplementary File 4), 4 individuals with *de novo* heterozygous *NEUROD2* mutations including 2 non-synonymous (comprising family 5) and 2 synonymous, and 1 non consanguineous family (6/8 individuals affected, family 6) with a paternal inherited *NEUROD2* heterozygous missense mutation (Fig. 7a,b). We also gained access to two previously reported cases carrying *de novo* heterozygous missense *NEUROD2* mutations [1] (families 3 and 4). All affected *NEUROD2* patients had globally normal brain MRI (Fig. 5c) but presented clinically with a spectrum of phenotypes including ID and ASD with or without ADHD/aggressiveness, epilepsy and/or developmental delay (Table 2). Patients carrying missense and synonymous *NEUROD2* mutations were identified by whole-exome sequencing and were confirmed by targeted Sanger sequencing of patients, parents and siblings DNA. These *NEUROD2* mutations were not found in any of the 141,456 individuals from gnomAD, and in all of our patients no other variants besides the *NEUROD2* mutations were identified in known disease-

causing genes that could account for the clinical phenotypes. Patients 3 (family 3) and 4 (family 4) who carry *de novo* E130Q or M134T mutation respectively, were analyzed as infants in a study associating *NEUROD2* with early infantile epilepsy [1], while in contrast the R129W and H268Q mutations were identified in this study. The R129W mutation found in patient 5 (family 5) is *de novo* while the H268Q mutation in patient 6-1, 6-2 and 6-3 (family 6) is inherited from their affected father. Strikingly, the heterozygous H268Q mutation was not found in the mother and the healthy brother 6-4, supporting a causal relationship between the *NEUROD2* mutation and the disease in this family.

E130Q, M134T and R129W mutations are localized in the DNA-binding basic domain of NEUROD2 protein (Fig. 7a). In contrast, the H268Q mutation is in the conserved Neuronal bHLH protein domain (Fig.7a).

To test the pathogenicity of *NEUROD2* R129W and H268Q mutations found in patients 5 (family 5) and 6-1 to 6-3 (family 6), we took advantage of the fact that human *NEUROD2* WT transfected in P19 embryonic carcinoma cells can induce differentiation into neurons [63]. While human WT *NEUROD2* was able to induce neuronal differentiation in ~ 90% of transfected cells, the R129W or H268Q mutations were not or less able to direct neuronal differentiation, respectively (~19 and 35% of transfected cells, respectively; Fig. 7d-f). These data indicate that both *NEUROD2* mutations are loss-of-function. In parallel we tested 3 other *NEUROD2* variants identified by whole exome sequencing in ASD/ID sporadic patients that had a priori lower pathogenic properties since two were synonymous (c.147G>A, p.P49=; c.930A>G, p.S310=) and the third was located on the last amino-acid on the N-terminal side of *NEUROD2* (c.1144A>C, p.N382H). As expected, our *in vitro* test showed normal capacity of these three variants to generate neurons (~ 90% of transfected cells, Fig. 7e,f), indicating that they are indeed non-pathogenic and excluding *NEUROD2* as the causative gene in these patients.

Patient	1	2	3 (from Sega et al., 2018)	4 (from Sega et al., 2018)	5	6-1
Mutation	1.57 Mb deletion (55 genes)	0.79 Mb deletion (37 genes)	c.388G>C; p.E130Q	c.401T>C, p.M134T	c.385C>T : p.R129W	c.804C>A : p.H268Q
Sex	Female	Male	Female	Male	Female	Male
Age	19 years	9 years	5 years	3.8 years	11 years	5 years
Inheritance	De novo	De novo	De novo	De novo	De novo	From affected father
Birth weight (g)	1300	2400	3175	unknown	4000	3402
Birth length (cm)	38	unknown	unknown	unknown	unknown	50.8
Birth head circumference (cm)	29	unknown	unknown	unknown	unknown	unknown
Age at last examination (years)	18	9	4.5	3.4	9	3
Weight at last examination (kg)	51	Not collected	<1% (Z=-2.47)	37 %-ile	>+2.5 SD	46.9
Height at last examination (cm)	149	Not collected	<1% (Z= -2.63)	41 %-ile	-1 SD	165.2
Head circumference at last examination (cm)	52	52	<1% (Z= - 2.49)	93%-ile	53	54.3
Failure to thrive	Yes	No	Yes	Yes	No	No
Head control	Delayed	Normal	Delayed (3.5 years)	Delayed (18 months)	Normal	Normal
Walking	Delayed (2 years)	Delayed (3 years 6 months)	Supported walking with walker, no unsupported walking	Delayed (2 year 6 months)	Normal (14 months)	Normal
Epilepsy	Yes	No	Infantile spasms from 5 months, ketogenic diet at 16 months and seizure-free since 2.5 years of age	Infantile spasms from 5 months, seizure-free since vagal nerve stimulation at 16 months	No	No
ID	Yes	Non testable (does not speak), but likely Yes	Too young to test but strongly reduced developmental quotient so likely Yes	Too young to test but reduced developmental quotient so likely Yes	Yes	Yes
Speech impairment	Yes	Yes, no verbal expression	Yes (5 single words only, no sentences)	at 3-years-5-months has vocalizations but not much consonants or intentional vowels	Yes (onset at 3)	Yes (single words only)
ASD	Yes, mainly stereotypic behavior	Yes	unclear	Too young to diagnose but lacks reciprocal play and imitation, thus is considered "at risk" for autism	Yes	Yes
ADHD/aggressive behavior	No	Agitated, hits his head, aggressive to himself and towards others, screams	Hyperkinetic and stereotypical movements	Hyperactive and repetitive behaviors, likes to pat things and to rock back and forth	No	Hyperactive and aggressive
MRI results	Mildly enlarged Virchow-Robin space	Normal	bilateral increased T2 signal intensities in putamina, parietal periventricular white matter, diffuse thinning of corpus callosum	At 10 months: mild, generalized cerebral volume loss, absence of the posterior pituitary T1 bright spot	Normal	NA
Associated malformations	None	None	None	None	None	None
Other clinical features	Atrium septal defect, unilateral kidney dysplasia, syrinx in spine with secondary spasticity of the left leg, unilateral corral leukoma, hypothyroidism	Mild unspecific facial dysmorphism (low implanted ears), asthma	Bilateral esotropia	Dysphagia, thickened feed	Central obesitas, large (long) frontal teeth, tapering fingers	Inverted nipples, clumsy

Table 2: Characteristics of patients with *NEUROD2* mutations

Footnote: ASD, autism spectrum disorder; ID, intellectual disability; MRI, magnetic resonance imaging; NA, data not available

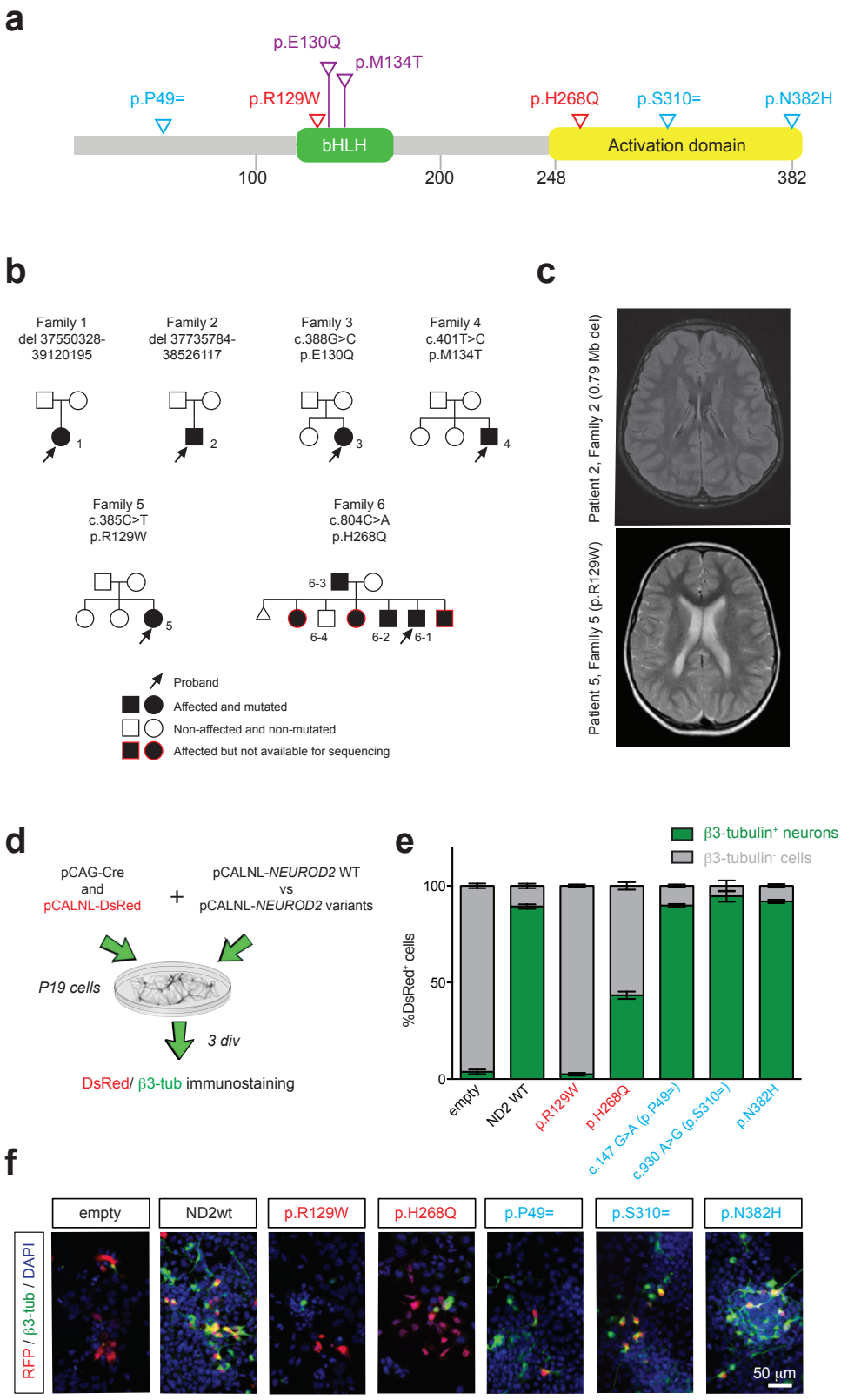

Figure 7: Loss-of-function variants of *NEUROD2* are associated with neuropsychiatric disorders

(a) Scheme depicting NEUROD2 mutations analyzed in this study, that are associated with ID/ASD. In red, novel pathogenic mutations; in blue, novel non-pathogenic mutations; in

purple, pathogenic mutations from Sega et al. [1]. (b) Pedigrees of 6 families with *NEUROD2* disruptions (Family 1 and 2 with copy number variations, Families 3 to 6 with the 4 pathogenic missense heterozygous mutations). Patients 6-1 and 6-2 in family 6 share the same mutation with their father (patient 6-3). Sanger sequencing showed that their healthy brother 6-4 does not carry the mutation in *NEUROD2*. (c) Axial T2-weighted MRI images of patients 2 and 5 showing no obvious abnormality in brain organization. (d-f) An *in vitro* test allowed to measure the pathogenicity of *NEUROD2* variants. (d) P19 cells were transfected with pCAG-Cre, pCALNL-RFP and a plasmid containing different variants of Cre-dependent human *NEUROD2* (pCALNL-*NEUROD2*). (e) We counted the percentage of RFP^+ cells expressing β3-tubulin in each condition. (f) Representative images of RFP-transfected neurons immunostained for β3-tubulin after 3 days *in vitro*.

Discussion

In this study, we examined the roles of the transcription factor NeuroD2 in the developing and adult cerebral cortex and discovered a critical role for this gene in neurobehavioral functions in mice and humans.

Migration and lamination phenotypes

First, our data indicate that NeuroD2 regulates radial migration of CPN precursor cells, with cells migrating more superficially in KO mice than in WT mice. Conversely, NeuroD2 overexpression in CPNs of WT mice resulted in an opposite phenotype, i.e. reduced migration, indicating that NeuroD2 regulates CPN migration in a cell autonomous manner. Factors downstream of NeuroD2 responsible for this migratory phenotype are likely to be found among NeuroD2-bound genes identified by Chip-seq during CPN migration [64]. At the mechanistic level, whether NeuroD2 regulates multipolar-bipolar transition, glia-guided migration velocity and/or terminal translocation remains to be investigated.

Similar to our study, accelerated or excessive CPN migration has been reported after IUE overexpression of APP [65], Rac1 and its interactor POSH [66] or Camk2b [67]. For APP

overexpression, over-migration was transient since it was not visible anymore at 6 days post-electroporation. This indicates that APP promotes migration velocity but not final laminar positioning of CPNs. For Rac1, POSH and Camk2b however, the long-term impact of their overexpression on final cortical lamination has remained unexplored [65-67]. Here CPN over-migration in NeuroD2 null mice was followed by a dorsal extension of deep layers at the expense of superficial layers, the latter being in turn compressed below the pial surface. The final cortical thickness and number of CPN subtypes were unaltered; as a result, PN subtypes displayed abnormally low *vs* high cell densities in deep *vs* superficial layers, respectively. This is to our knowledge the first time that such a phenotype is described. Given that even slight alterations in CPN positioning are sufficient to alter cortical output [68,69], it is expected that this laminar positioning phenotype participates in disrupting cortical function.

NeuroD2 as a specific synapse-regulating factor among NeuroD family members?

We did not observe any obvious axonal targeting defects in NeuroD2 null mice, strongly contrasting with the absence of corpus callosum in NeuroD2/NeuroD6 double mutant animals [21]. A likely explanation resides in the functional redundancy between NeuroD family members concerning axon growth and navigation. In contrast, it seems plausible that the observed synaptic phenotypes are due specifically to NeuroD2 deletion among other NeuroD family members. This hypothesis is supported by the fact that NeuroD2 is the only NeuroD family member that has been linked to synaptic integration [12,20,37,70].

Generic and layer-specific phenotypes in *NeuroD2* KO cortex

This study reveals that some electrophysiological phenotypes might be specific to CPN subtypes while other might be generic. First, although NeuroD2 is expressed in CPNs of all layers at P30, L2/3 CPNs in *NeuroD2* KO mice display reduced frequencies of both mEPSCs and mIPSCs with normal amplitudes [20], while L5 CPNs show increased mIPSC amplitude (this study). Thus, NeuroD2 deletion alters synaptic properties differently in different CPNs. However, intrinsic excitability was increased similarly in both L2/3 and L5 CPNs of *NeuroD2*

KO mice, suggesting that excitability control is a more universal function of NeuroD2. This is consistent with unpublished preliminary results showing increased excitability of hippocampal CA1 PNs in *NeuroD2* KO mice *in vivo* (Jérôme Epsztein, personal communication). Nevertheless, the mechanisms by which NeuroD2 regulates intrinsic excitability in L2/3 and L5 CPNs are likely different since decreased AHP was found as an underlying cause in L2/3 [20] but was unmodified in L5 CPNs (this study). The molecular mechanisms underlying increased L5 neuron excitability in NeuroD2 mutants require further investigations.

Mechanistic insights of *NeuroD2* KO phenotypes from RNA-seq analyses

A literature-based research of our P30 DEX gene list suggests a large number of possible *NeuroD2* targets that might regulate the cellular and behavioral phenotypes described in the study. For example, downregulation of the glucocorticoid receptor *Nr3c1* (also called *GR*) and/or of the synaptome gene *Syne1* (CPG isoform) in *NeuroD2* KO mice might account for the spine density reduction at P30. First, GR is a critical regulator of spine development and plasticity in cortical PN apical dendrites [71], a compartment where spine density was most affected in *NeuroD2* KO mice. Short and long term stresses both preferentially alter spine formation in the apical tuft of cortical PNs, through glucocorticoid binding to GR in L1 [72], which then induces a ligand-dependent internalization and transcription factor activity of *GR*. Furthermore, a recent study indicated that DNA-bound *GR* requires *NeuroD2* as a cofactor to transactivate its target genes [73]. Together with the current discovery that NeuroD2 induces *GR* transcription at P30, these data suggest that *NeuroD2* is required for stress-induced synaptic plasticity in CPN apical dendrites. This hypothesis is corroborated by the fact that *NeuroD2* KO mice show reduced fear behavior in the elevated plus maze, in fear conditioning tasks [10] and in conflict anxiety (this study), and by the fact that some of the patients with *NEUROD2* pathogenic variants depicted here show hyperactive/aggressive behavior. Besides *GR*, *CPG2*, a gene that is downregulated in null mice, encodes an actin-binding protein that regulates activity-dependent glutamate receptor endocytosis [74] and RNA transport to nascent postsynaptic sites [74]. Interestingly, pathogenic variants in *CPG2* are associated with bipolar

disorders [75]. However, other candidates among the 37 post-synaptic genes might as well participate in the spine phenotype of null mice.

Concerning locomotor hyperactivity and spontaneous epilepsy observed in *NeuroD2* KO mice, good candidate genes lie among the 13 DEX voltage-gated ion channels, for example *Kcnq5* and *Scn8a*. *Kcnq5* is a L5 enriched potassium channel [76,77] (Allen Brain Atlas) and the *Scn8a* sodium channel that regulates dendritic excitability in CPNs [78], and both have been implicated in epilepsy and/or hyperactivity.

The increased mIPSC amplitude in L5 CPNs of *NeuroD2* KO mice suggests increased expression or trafficking of post-synaptic GABA-A receptors; however, we did not identify an obvious DEX gene that could account for this phenotype in our gene list. Nevertheless, there has been rapid advancement in single-cell transcriptomic technologies, and studying the transcriptomic changes occurring selectively in this specific CPN subtype may provide insight into the mechanisms for this increased mIPSC amplitude. Alternatively, the increased mIPSC amplitude in L5 CPNs might be due to changes in electrotonic, passive membrane properties associated with the observed increased input resistance.

Concerning increased Ih current density in L5 CPNs, a likely candidate gene from our RNA-seq screen is *Trip8b*. *Trip8b* is a critical regulator of membrane localization and expression of HCN1 channels that induce Ih current density [79,80]. Independently of its mechanism, increased Ih currents tend to decrease intrinsic neuronal excitability, suggesting that this phenotype is not part of initial defects but instead might represent a compensatory mechanism to reduce neuronal hyperexcitability [40]. The large number of DEX genes that can possibly account for the phenotypes observed in null mice renders functional rescue experiments impractical, but cell type specific *NeuroD2* deletion will help discover the implicated genes.

Which brain region is involved in each behavioral defect?

The behavioral deficits of *NeuroD2* KO mice might be due to cerebral cortex phenotypes described here, but other NeuroD2-expressing brain regions can also be involved. In particular, while hyperactivity [69] and conflict anxiety [61] might rely essentially on the functional integrity of

the cerebral cortex, social interactions and social memory deficits might also depend on the hippocampus, amygdala, hypothalamus or cerebellum, that all contain NeuroD2-expressing cells. This hypothesis is strengthened by reduced synaptic density in hippocampal neuron subsets [37] and lower amygdala size [10] in NeuroD2 null mice. Mice with conditional NeuroD2 deletions will be instrumental in deciphering the relative contributions of specific brain regions and cell types in selected behavioral deficits.

NEUROD2 mutations induce specific neuropsychiatric disorders

Our data from mice and humans clarify the expected phenotype for patients carrying a *NEUROD2* mutation. Indeed by combining and comparing our clinical data with a previously published study [1] the NEUROD2 phenotype can be centered on ID and ASD with speech impairment although it can also be accompanied by ADHD and/or epilepsy. Importantly, novel *NEUROD2* variants can now be easily tested for pathogenicity using the *in vitro* assay we describe here, which is both simple and efficient. Also, the DECIPHER database reports a small, 135 kb-long duplication encompassing *NEUROD2* that is associated with ID and attention deficit. This suggests that not only too low but also too high expression levels of *NEUROD2* is potentially detrimental and that both variations generate similar symptoms, similar to what has been reported concerning *MECP2* [81] or *SHANK3* [82,83].

For the first time we show compelling evidence that NeuroD2 is necessary for the development of normal social behavior and for the control of locomotor activity levels in mice and humans. These data are in agreement with many established mouse models of ASD [84,85], but social memory impairment and hyperactivity are also typical features of SCZ and SCZ mouse models [86,87]. Given that the SCZ risk genes *TCF4* and *MIR-137* are potential NeuroD2 interacting molecules, it will be interesting to seek for SCZ patients with NeuroD2 variants.

Perspectives

In vitro pieces of evidence have suggested a link between *NeuroD2* and neuronal activity. Indeed, NeuroD2 transactivation is increased by activity in cultured cortical neurons [12], and

NeuroD2 mRNA expression is regulated by NMDAR activation [70]. In this context, it will be important to test whether and how NeuroD2 regulates experience-dependent neuronal and synaptic plasticity *in vivo*, and how this relates to neuropsychiatric disorders.

Acknowledgements:

This work was supported by the Agence Nationale de la Recherche (ANR-13-JSV4-0006 to A.d.C. and ANR-13-BSV4-0013-01 to H.C.), the Fondation Pour la Recherche sur le Cerveau and the Fondation Lejeune (both to A.d.C.), the European Community 7th Framework programs (Development and Epilepsy—Strategies for Innovative Research to improve diagnosis, prevention and treatment in children with difficult to treat Epilepsy [DESIRE] (to A.d.C., C.C and A.R.). High throughput sequencing was performed at the TGML Platform, supported by grants from Inserm, GIS IBiSA, Aix-Marseille Université, and ANR-10-INBS-0009-10. Financial support to S.B. was provided by the Fondation Pour la Recherche Médicale. We thank the PPGI, PBMC and InMAGIC platforms at INMED for their important technical support, O.J. Manzoni and P. Chavis for advice along the course of the study, Bruno Pichon and Audrey Van Hecke for assistance in genetic and clinical data, respectively.

Author contributions:

A.d.C. and H.C. conceived and initiated the project. K.R., R.M. S.B. and A.d.C. conceived and designed all the experiments. A.R., H.C. and C.C. provided critical input to the project at all steps. K.R., R.M., S.B., S.L., C.B., S.S., F.S., A.L., L.H., S.G., M.C., E.P.P., A.M. and A.d.C. performed the experiments. Lamination experiments were done by R.M. and K.R.; migration experiments by K.R. and F.S., spine density experiments by S.L. and A.d.C., spine turnover experiments by S.B., electrophysiological synaptic properties experiments by S.S., intrinsic neuronal properties by C.B., RNAseq experiments by S.L., L.H. and A.d.C., behavior by S.G. (Phenotype Expertise), qPCR and Sanger sequencing by E.P.P. and A.M. and *in vitro* pathogenicity testing experiments by E.P.P., R.M. and A.d.C. All analyzes were performed by

K.R., R.M., S.B. or A.d.C. Scientific discussions and collaborative experiments with A.B. grounded the project. J.A.R., E.H., K.L., S.M.A., L.J., A.V.H., O.V., B.P., A.V.H., D.A., S.K., and C.G. recruited patients, acquired clinical data, or analyzed whole-exome or Sanger sequencing results. K.R., R.M., S.B. and A.d.C. drafted the original manuscript, and all authors assisted in editing the manuscript.

Conflicts of interest:

The authors declare no conflict of interest.

Supplementary information is available at MP's website.

References:

1. Sega, A.G. *et al.* De novo pathogenic variants in neuronal differentiation factor 2 (NEUROD2) cause a form of early infantile epileptic encephalopathy. *J Med Genet* **56**, 113-122 (2019).
2. Spellmann, I. *et al.* Associations of NEUROD2 polymorphisms and change of cognitive dysfunctions in schizophrenia and schizoaffective disorder after eight weeks of antipsychotic treatment. *Cogn Neuropsychiatry* **22**, 280-297 (2017).
3. Willsey, A.J. *et al.* Coexpression networks implicate human midfetal deep cortical projection neurons in the pathogenesis of autism. *Cell* **155**, 997-1007 (2013).
4. Raedler, T.J., Knable, M.B. & Weinberger, D.R. Schizophrenia as a developmental disorder of the cerebral cortex. *Curr Opin Neurobiol* **8**, 157-61 (1998).
5. Zoghbi, H.Y. & Bear, M.F. Synaptic dysfunction in neurodevelopmental disorders associated with autism and intellectual disabilities. *Cold Spring Harb Perspect Biol* **4**(2012).
6. Rubenstein, J.L. & Merzenich, M.M. Model of autism: increased ratio of excitation/inhibition in key neural systems. *Genes Brain Behav* **2**, 255-67 (2003).
7. Fernandez, F. & Garner, C.C. Over-inhibition: a model for developmental intellectual disability. *Trends Neurosci* **30**, 497-503 (2007).
8. Lee, J.E. *et al.* Conversion of Xenopus ectoderm into neurons by NeuroD, a basic helix-loop-helix protein. *Science* **268**, 836-44 (1995).
9. McCormick, M.B. *et al.* NeuroD2 and neuroD3: distinct expression patterns and transcriptional activation potentials within the neuroD gene family. *Mol Cell Biol* **16**, 5792-800 (1996).
10. Lin, C.H. *et al.* The dosage of the neuroD2 transcription factor regulates amygdala development and emotional learning. *Proc Natl Acad Sci U S A* **102**, 14877-82 (2005).
11. Yang, Y. *et al.* A Cdc20-APC ubiquitin signaling pathway regulates presynaptic differentiation. *Science* **326**, 575-8 (2009).
12. Ince-Dunn, G. *et al.* Regulation of thalamocortical patterning and synaptic maturation by NeuroD2. *Neuron* **49**, 683-95 (2006).
13. Cross-Disorder Group of the Psychiatric Genomics, C. Identification of risk loci with shared effects on five major psychiatric disorders: a genome-wide analysis. *Lancet* **381**, 1371-9 (2013).
14. Ripke, S. *et al.* Genome-wide association analysis identifies 13 new risk loci for schizophrenia. *Nat Genet* **45**, 1150-9 (2013).
15. Amiel, J. *et al.* Mutations in TCF4, encoding a class I basic helix-loop-helix transcription factor, are responsible for Pitt-Hopkins syndrome, a severe epileptic encephalopathy associated with autonomic dysfunction. *Am J Hum Genet* **80**, 988-93 (2007).
16. Brockschmidt, A. *et al.* Severe mental retardation with breathing abnormalities (Pitt-Hopkins syndrome) is caused by haploinsufficiency of the neuronal bHLH transcription factor TCF4. *Hum Mol Genet* **16**, 1488-94 (2007).
17. Zweier, C. *et al.* Haploinsufficiency of TCF4 causes syndromal mental retardation with intermittent hyperventilation (Pitt-Hopkins syndrome). *Am J Hum Genet* **80**, 994-1001 (2007).
18. Ravanpay, A.C. & Olson, J.M. E protein dosage influences brain development more than family member identity. *J Neurosci Res* **86**, 1472-81 (2008).
19. Krishnan, A. *et al.* Genome-wide prediction and functional characterization of the genetic basis of autism spectrum disorder. *Nat Neurosci* **19**, 1454-1462 (2016).
20. Chen, F. *et al.* The transcription factor NeuroD2 coordinates synaptic innervation and cell intrinsic properties to control excitability of cortical pyramidal neurons. *J Physiol* **594**, 3729-44 (2016).
21. Bormuth, I. *et al.* Neuronal basic helix-loop-helix proteins Neurod2/6 regulate cortical commissure formation before midline interactions. *J Neurosci* **33**, 641-51 (2013).
22. Pieper, A. *et al.* NeuroD2 controls inhibitory circuit formation in the molecular layer of the cerebellum. *Sci Rep* **9**, 1448 (2019).

23. de Chevigny, A. *et al.* miR-7a regulation of Pax6 controls spatial origin of forebrain dopaminergic neurons. *Nat Neurosci* **15**, 1120-6 (2012).
24. Rodriguez, A., Ehlenberger, D.B., Dickstein, D.L., Hof, P.R. & Wearne, S.L. Automated three-dimensional detection and shape classification of dendritic spines from fluorescence microscopy images. *PLoS One* **3**, e1997 (2008).
25. Huang da, W., Sherman, B.T. & Lempicki, R.A. Systematic and integrative analysis of large gene lists using DAVID bioinformatics resources. *Nat Protoc* **4**, 44-57 (2009).
26. Bindea, G. *et al.* ClueGO: a Cytoscape plug-in to decipher functionally grouped gene ontology and pathway annotation networks. *Bioinformatics* **25**, 1091-3 (2009).
27. Gascon, E. *et al.* Alterations in microRNA-124 and AMPA receptors contribute to social behavioral deficits in frontotemporal dementia. *Nat Med* **20**, 1444-51 (2014).
28. Farah, M.H. *et al.* Generation of neurons by transient expression of neural bHLH proteins in mammalian cells. *Development* **127**, 693-702 (2000).
29. Telley, L. *et al.* Sequential transcriptional waves direct the differentiation of newborn neurons in the mouse neocortex. *Science* **351**, 1443-6 (2016).
30. Lodato, S. *et al.* Excitatory projection neuron subtypes control the distribution of local inhibitory interneurons in the cerebral cortex. *Neuron* **69**, 763-79 (2011).
31. Rouaux, C. & Arlotta, P. Direct lineage reprogramming of post-mitotic callosal neurons into corticofugal neurons in vivo. *Nat Cell Biol* **15**, 214-21 (2013).
32. Ye, Z. *et al.* Instructing Perisomatic Inhibition by Direct Lineage Reprogramming of Neocortical Projection Neurons. *Neuron* **88**, 475-83 (2015).
33. Shepherd, G.M. Corticostriatal connectivity and its role in disease. *Nat Rev Neurosci* **14**, 278-91 (2013).
34. Oswald, M.J., Tantirigama, M.L., Sonntag, I., Hughes, S.M. & Empson, R.M. Diversity of layer 5 projection neurons in the mouse motor cortex. *Front Cell Neurosci* **7**, 174 (2013).
35. Cubelos, B. *et al.* Cux1 and Cux2 regulate dendritic branching, spine morphology, and synapses of the upper layer neurons of the cortex. *Neuron* **66**, 523-35 (2010).
36. Falace, A. *et al.* TBC1D24 regulates neuronal migration and maturation through modulation of the ARF6-dependent pathway. *Proc Natl Acad Sci U S A* **111**, 2337-42 (2014).
37. Wilke, S.A. *et al.* NeuroD2 regulates the development of hippocampal mossy fiber synapses. *Neural Dev* **7**, 9 (2012).
38. Feng, G. *et al.* Imaging neuronal subsets in transgenic mice expressing multiple spectral variants of GFP. *Neuron* **28**, 41-51 (2000).
39. Fenelon, K. *et al.* The pattern of cortical dysfunction in a mouse model of a schizophrenia-related microdeletion. *J Neurosci* **33**, 14825-39 (2013).
40. Benarroch, E.E. HCN channels: function and clinical implications. *Neurology* **80**, 304-10 (2013).
41. Sheets, P.L. *et al.* Corticospinal-specific HCN expression in mouse motor cortex: I(h)-dependent synaptic integration as a candidate microcircuit mechanism involved in motor control. *J Neurophysiol* **106**, 2216-31 (2011).
42. Carr, D.B., Andrews, G.D., Glen, W.B. & Lavin, A. alpha2-Noradrenergic receptors activation enhances excitability and synaptic integration in rat prefrontal cortex pyramidal neurons via inhibition of HCN currents. *J Physiol* **584**, 437-50 (2007).
43. Pereanu, W. *et al.* AutDB: a platform to decode the genetic architecture of autism. *Nucleic Acids Res* (2017).
44. Darnell, J.C. *et al.* FMRP stalls ribosomal translocation on mRNAs linked to synaptic function and autism. *Cell* **146**, 247-61 (2011).
45. Inlow, J.K. & Restifo, L.L. Molecular and comparative genetics of mental retardation. *Genetics* **166**, 835-81 (2004).
46. Lubs, H.A., Stevenson, R.E. & Schwartz, C.E. Fragile X and X-linked intellectual disability: four decades of discovery. *Am J Hum Genet* **90**, 579-90 (2012).
47. Ropers, H.H. Genetics of intellectual disability. *Curr Opin Genet Dev* **18**, 241-50 (2008).

48. van Bokhoven, H. Genetic and epigenetic networks in intellectual disabilities. *Annu Rev Genet* **45**, 81-104 (2011).
49. Schizophrenia Working Group of the Psychiatric Genomics, C. Biological insights from 108 schizophrenia-associated genetic loci. *Nature* **511**, 421-7 (2014).
50. Pirooznia, M. *et al.* SynaptomeDB: an ontology-based knowledgebase for synaptic genes. *Bioinformatics* **28**, 897-9 (2012).
51. Ryan, B.C., Young, N.B., Crawley, J.N., Bodfish, J.W. & Moy, S.S. Social deficits, stereotypy and early emergence of repetitive behavior in the C58/J inbred mouse strain. *Behav Brain Res* **208**, 178-88 (2010).
52. Silverman, J.L., Yang, M., Lord, C. & Crawley, J.N. Behavioural phenotyping assays for mouse models of autism. *Nat Rev Neurosci* **11**, 490-502 (2010).
53. Olson, J.M. *et al.* NeuroD2 is necessary for development and survival of central nervous system neurons. *Dev Biol* **234**, 174-87 (2001).
54. van Ool, J.S. *et al.* A systematic review of neuropsychiatric comorbidities in patients with both epilepsy and intellectual disability. *Epilepsy Behav* **60**, 130-137 (2016).
55. Canitano, R. Epilepsy in autism spectrum disorders. *Eur Child Adolesc Psychiatry* **16**, 61-6 (2007).
56. Cascella, N.G., Schretlen, D.J. & Sawa, A. Schizophrenia and epilepsy: is there a shared susceptibility? *Neurosci Res* **63**, 227-35 (2009).
57. Ahuja, A., Martin, J., Langley, K. & Thapar, A. Intellectual disability in children with attention deficit hyperactivity disorder. *J Pediatr* **163**, 890-5 e1 (2013).
58. Han, S. *et al.* Autistic-like behaviour in Scn1a+/- mice and rescue by enhanced GABA-mediated neurotransmission. *Nature* **489**, 385-90 (2012).
59. Rao, P.A. & Landa, R.J. Association between severity of behavioral phenotype and comorbid attention deficit hyperactivity disorder symptoms in children with autism spectrum disorders. *Autism* **18**, 272-80 (2014).
60. Gough, A. & Morrison, J. Managing the comorbidity of schizophrenia and ADHD. *J Psychiatry Neurosci* **41**, E79-80 (2016).
61. Weisstaub, N.V. *et al.* Cortical 5-HT2A receptor signaling modulates anxiety-like behaviors in mice. *Science* **313**, 536-40 (2006).
62. Crawley, J.N. Mouse behavioral assays relevant to the symptoms of autism. *Brain Pathol* **17**, 448-59 (2007).
63. Gonzalez-Maeso, J. *et al.* Identification of a serotonin/glutamate receptor complex implicated in psychosis. *Nature* **452**, 93-7 (2008).
64. Bayam, E. *et al.* Genome-wide target analysis of NEUROD2 provides new insights into regulation of cortical projection neuron migration and differentiation. *BMC Genomics* **16**, 681 (2015).
65. Young-Pearse, T.L. *et al.* A critical function for beta-amyloid precursor protein in neuronal migration revealed by in utero RNA interference. *J Neurosci* **27**, 14459-69 (2007).
66. Yang, T. *et al.* POSH localizes activated Rac1 to control the formation of cytoplasmic dilation of the leading process and neuronal migration. *Cell Rep* **2**, 640-51 (2012).
67. Nicole, O. *et al.* A novel role for CAMKIIbeta in the regulation of cortical neuron migration: implications for neurodevelopmental disorders. *Mol Psychiatry* **23**, 2209-2226 (2018).
68. Nakagawa, J.M. *et al.* Characterization of focal cortical dysplasia with balloon cells by layer-specific markers: Evidence for differential vulnerability of interneurons. *Epilepsia* **58**, 635-645 (2017).
69. Lu, H.C. *et al.* Disruption of the ATXN1-CIC complex causes a spectrum of neurobehavioral phenotypes in mice and humans. *Nat Genet* **49**, 527-536 (2017).
70. Chen, F. & Hall, B.J. Synaptic activity suppresses expression of neurogenic differentiation factor 2 in an NMDA receptor-dependent manner. *Synapse* **71**(2017).
71. Liston, C. & Gan, W.B. Glucocorticoids are critical regulators of dendritic spine development and plasticity in vivo. *Proc Natl Acad Sci U S A* **108**, 16074-9 (2011).

72. Brown, S.M., Henning, S. & Wellman, C.L. Mild, short-term stress alters dendritic morphology in rat medial prefrontal cortex. *Cereb Cortex* **15**, 1714-22 (2005).
73. van Weert, L. *et al.* NeuroD Factors Discriminate Mineralocorticoid From Glucocorticoid Receptor DNA Binding in the Male Rat Brain. *Endocrinology* **158**, 1511-1522 (2017).
74. Packard, M. *et al.* Nucleus to Synapse Nesprin1 Railroad Tracks Direct Synapse Maturation through RNA Localization. *Neuron* **86**, 1015-1028 (2015).
75. Rathje, M. *et al.* Genetic variants in the bipolar disorder risk locus SYNE1 that affect CPG2 expression and protein function. *Mol Psychiatry* (2019).
76. Molyneaux, B.J. *et al.* DeCoN: genome-wide analysis of in vivo transcriptional dynamics during pyramidal neuron fate selection in neocortex. *Neuron* **85**, 275-288 (2015).
77. Lehman, A. *et al.* Loss-of-Function and Gain-of-Function Mutations in KCNQ5 Cause Intellectual Disability or Epileptic Encephalopathy. *Am J Hum Genet* **101**, 65-74 (2017).
78. Lorincz, A. & Nusser, Z. Molecular identity of dendritic voltage-gated sodium channels. *Science* **328**, 906-9 (2010).
79. Santoro, B. *et al.* TRIP8b splice variants form a family of auxiliary subunits that regulate gating and trafficking of HCN channels in the brain. *Neuron* **62**, 802-13 (2009).
80. Piskorowski, R., Santoro, B. & Siegelbaum, S.A. TRIP8b splice forms act in concert to regulate the localization and expression of HCN1 channels in CA1 pyramidal neurons. *Neuron* **70**, 495-509 (2011).
81. Lu, H. *et al.* Loss and Gain of MeCP2 Cause Similar Hippocampal Circuit Dysfunction that Is Rescued by Deep Brain Stimulation in a Rett Syndrome Mouse Model. *Neuron* **91**, 739-747 (2016).
82. Han, K. *et al.* SHANK3 overexpression causes manic-like behaviour with unique pharmacogenetic properties. *Nature* **503**, 72-7 (2013).
83. Durand, C.M. *et al.* Mutations in the gene encoding the synaptic scaffolding protein SHANK3 are associated with autism spectrum disorders. *Nat Genet* **39**, 25-7 (2007).
84. Ferguson, J.N. *et al.* Social amnesia in mice lacking the oxytocin gene. *Nat Genet* **25**, 284-8 (2000).
85. Peca, J. *et al.* Shank3 mutant mice display autistic-like behaviours and striatal dysfunction. *Nature* **472**, 437-42 (2011).
86. Piskorowski, R.A. *et al.* Age-Dependent Specific Changes in Area CA2 of the Hippocampus and Social Memory Deficit in a Mouse Model of the 22q11.2 Deletion Syndrome. *Neuron* **89**, 163-76 (2016).
87. van den Buuse, M. Modeling the positive symptoms of schizophrenia in genetically modified mice: pharmacology and methodology aspects. *Schizophr Bull* **36**, 246-70 (2010).

Most appropriate position for Table 1: after or in the middle of the Result paragraph subheaded **"**NeuroD2 target genes show a strong enrichment in voltage-sensitive ion channel activity, synapse modulation, ASD and SCZ".

Most appropriate position for Table 2: before the discussion.

Supplementary Videos 1 and 2 footnote: Behavioral seizures in 2 *NeuroD2* KO mice videotaped while the open field test was performed. Behavioral seizures were captured on video in two mice. In mouse #215-106, seizure manifested as a sudden stop of exploratory behavior and brief myoclonic jerks (1-2 sec), immediately followed by a myoclonic seizure (10sec) with total loss of quadruped posture. During myoclonic seizure, mouse #215-106 exhibited repeated clonic jerks of the limbs while lying on its side in a curled-up position. Episode stopped after ~10sec when the mouse recovered postural control, and was followed by 1-2min of hypoactivity. In mouse #215-088, seizure started with neck jerks, followed by a brief period (6-7sec) with rearing and forelimb clonus. Seizure behavior quickly progressed to a high intensity stage of wild jumps that stopped after ~25sec, and the mouse remained immobile/unresponsive for ~1min.

Figure 1: Altered laminar position and excess radial migration of CPNs in *NeuroD2* null mice.

(a-c) Cortical expression of NeuroD2 across development. (a) qPCR shows permanent cortical expression of *NeuroD2* mRNA with a peak expression at E18.5. (b) In situ hybridizations from Allen Brain Atlas confirm permanent *NeuroD2* mRNA expression across cortical layers and ages (S1 shown). (c) NeuroD2 protein expression at E18.5 and P28 in the S1 cortex.

(d-g) Number and laminar distribution of PNs from different cortical layers in NeuroD2 null mice. Tbr1$^+$ cortico-thalamic and Ctip2$^+$ subcortical PN layers extended superficially, at the expense of RORβ$^+$ and Cux1$^+$ superficial PNs that were compressed below the pial surface. Total number of Tbr1, Ctip2, RORβ and Cux1$^+$ cells per cortical column were unaltered, indicating unchanged production of PNs.

(h-i) NeuroD2 expression cell-autonomously regulates radial migration of L5 PNs during. (h) RFP-electroporated PNs settled more superficially in *NeuroD2* null mice compared with WT littermates. (i) Post-mitotic overexpression of NeuroD2 in PNs of WT mice induced a reduced migration of electroporated cells.

Data are represented as means ± SEM. Statistical significance was evaluated by Student t-test or Mann-Whitney test depending on normality of samples [(d)-(g)] or by two-way ANOVA followed by Bonferroni's post-hoc test [(d)-(i)] (*P < 0.05, **P < 0.01, ***P < 0.001, ****P < 0.0001).

Figure 2: Synaptic deficits in basal and apical dendrites of CPNs in *NeuroD2* KO mice.

(a,b) Total lengths of basal (a) and apical (b) dendrites of L5 CPNs were not significantly altered.

(c-e) Age-dependent spine density defects in basal dendrites. (d) Representative photomicrographs at P30 and P120 (scale bar 10 μm), (e) Subtle reduction in spine density at P30 but no difference P120. Note the significant spine density reduction between P30 and P120 in both genotypes. N= 16 dendritic segments from 3 WT mice and 33 segments from 7 KO mice at 1 month, 33 segments from 3 WT and 27 segments from 3 KO mice at 4 months.

(f-h) Age-dependent spine density defects in apical tuft dendrites. (g) Photomicrographs at P30 and P120 (scale bar 10 μm). (h) Quantification showing significant reduction of spine density at P30 but not P120.

(i-l) Increased acute spine gain and net spine formation in apical tuft dendrites at P30. (i) Experimental paradigm and representative images. Blue arrowheads depict lost spines while red arrowheads depict gained spines over 3 days. (j) Spine gain, (k) spine loss and (l) spine net formation. Data are represented as means ± SEM. Statistical analyses were performed using two-tailed t-tests or Mann-Whitney test depending on the normality of samples. *P < 0.05, **P < 0.01, ***P < 0.001, ****P < 0.0001.

Figure 3: Electrophysiological characterization of L5 CPNs in *NeuroD2* null mice.

(a-g) Miniature post-synaptic currents. Representative traces (b), frequency (c) and amplitude (d) of mEPSCs. Example traces (e), frequency (f) and amplitude (g) of mIPSCs. Amplitude of mIPSC was increased (g).

(h-j) Action potential properties, including Vrest (h), AP firing threshold (i) and AP amplitude (j). (k,l) Membrane resistance (k) and capacitance (l).

(m-n) Intrinsic excitability. Representative firing responses to +80 pA current steps in a WT (top) and a KO (down) cell. (n) *NeuroD2* KO neurons reached action potential (AP) firing threshold earlier than WT neurons and exhibited a steeper input-output relationship, as assessed by the number of APs elicited by increasing current injections (from +20 to +160 pA, 20-pA increments) during current-clamp recordings.

(o) After-hyperpolarization (AHP) was normal in L5 PNs of *NeuroD2* KO mice.

(p,q) *NeuroD2* KO L5 PNs exhibited increased Ih-current amplitudes compared with WT PNs (current/voltage relation of Ih currents). (p) shows experimental protocol and representative traces, (q) shows summary graph of the voltage-current relation.

Data are means ± SEM. Number of cells/ animals analyzed are shown in graphs in parentheses. Statistical significance was evaluated by unpaired t-test for samples with normal distributions [bar graphs in (b), (c), and (f)], by Mann-Whitney test for non-normal samples [bar

graph in (e)], and by two-way repeated measure ANOVA [(n) and (q)] followed by Bonferroni's post hoc test. *P < 0.05; **P < 0.01.

Figure 4: RNA-seq analysis of differentially expressed genes in motor/somatosensory cortex of P30 *NeuroD2* KO mice.

(a) Schematic of the experiment. (b) Validation of RNA-seq data by qPCR for several ion channel/ neuropsychiatric-related genes. N=3 experiments per genotype. (c) Venn diagram of DEX genes specific to L2/3, L5 and L6 (171 DEX genes are generic to all layers, some are common between 2 layers and others specific to a single layer). (d) Fold change expression (FC; log2 scale) of DEX genes belonging to specific layers, ranked according to adjusted P value (lowest Padj on top). (e) Results of gene set enrichment analysis using the DAVID knowledgebase. (f) Fold change expression (FC; log2 scale) of DEX genes belonging to the voltage-dependent ion channel family, ranked according to Padj (lowest on top). Genes associated with neuropsychiatric recurrent syndromes are depicted in blue. (g-i) Association of DEX genes with neuropsychiatric diseases. (g) Heatmap for synaptic and disease gene sets among DEX genes (red, higher expression; blue, lower expression). (h) Venn diagrams identifying overlaps between DEX genes and synaptic/disease gene sets. Number of genes for each gene set is indicated. (i) Graphical representation of % [DEX genes] (orange) vs % [same number of randomly selected genes] (grey) belonging to gene sets of interest. Statistical significance was evaluated by two-tailed Student t test [(b)] or binomial test [(i)] (*P < 0.05; **P < 0.01; ****P < 0.0001).

Figure 5: *NeuroD2* KO DEX genes associated with neuropsychiatric disorders. Fold change expression (FC; log2 scale) of DEX genes belonging to specific gene sets, ranked according to adjusted *P* value (lowest *P*adj on top). In the graph representing synaptome genes (SYN), presynaptic genes are depicted in light blue while postsynaptic genes are in dark blue.

Figure 6: Behavioral hallmarks of neuropsychiatric disorders in NeuroD2 mutant mice

(a-c) In the novel object recognition test (a), *NeuroD2* KO and HET mice displayed unaltered total investigation time (b) and discrimination index between the familiar and the novel object (c). (d-f) During social interaction in the three-chamber test (d), all genotypes displayed similar total social investigation time (e). However, while WT and HET mice spent around twice more time investigating the mouse than the empty quadrant, *NeuroD2* KO mice spent equivalent times investigating mouse and empty quadrants (f). (g-i) Social memory/ interest test. When a familiar and a novel mouse were placed in each quadrant (g), all genotypes spent similar times having social interactions (h), but only WT mice spent significantly more time investigating the novel mouse, indicating altered social memory in HET and KO mice (i). (j) Circling (left graph) and rearing (right graph) behaviors in the 3 genotypes. (k) Spontaneous seizures were observed in a third of *NeuroD2* KO mice and in one HET mouse during the behavioral experiments, but never in WT littermates. (l) Hyperactivity in *NeuroD2* KO mice. Left graph depicts the distance traveled in 1 minute-intervals during 10 minutes in the open field. Middle graph shows velocity during motion and right graph shows resting time, both during a 1-hour recording. N= 16 WT, 15 HET and 15 KO mice aged 8-14 weeks depending on the test. Data are means ± SEM. Statistical significance was evaluated by one-way ANOVA [(f), (g), (i), (l), (n) and (p)] or two-way ANOVA followed by Bonferroni's post hoc test [(j) and (m)] (n.s., not significant; **P* < 0.05; ***P* < 0.01; ****P* < 0.001).

Figure 7: Loss-of-function variants of *NEUROD2* are associated with neuropsychiatric disorders

(a) Scheme depicting NEUROD2 mutations analyzed in this study, that are associated with ID/ASD. In red, novel pathogenic mutations; in blue, novel non-pathogenic mutations; in purple, pathogenic mutations from Sega et al. [1]. (b) Pedigrees of 6 families with *NEUROD2* disruptions (Family 1 and 2 with copy number variations, Families 3 to 6 with the 4 pathogenic missense heterozygous mutations). Patients 6-1 and 6-2 in family 6 share the same mutation

with their father (patient 6-3). Sanger sequencing showed that their healthy brother 6-4 does not carry the mutation in *NEUROD2*. (c) Axial T2-weighted MRI images of patients 2 and 5 showing no obvious abnormality in brain organization. (d-f) An *in vitro* test allowed to measure the pathogenicity of *NEUROD2* variants. (d) P19 cells were transfected with pCAG-Cre, pCALNL-RFP and a plasmid containing different variants of Cre-dependent human *NEUROD2* (pCALNL-*NEUROD2*). (e) We counted the percentage of RFP^+ cells expressing β3-tubulin in each condition. (f) Representative images of RFP-transfected neurons immunostained for β3-tubulin after 3 days *in vitro*.

Figure S1: Developmental expression of NeuroD2 mRNA and protein in the mouse cerebral cortex. (a) NeuroD2 mRNA (purple) is expressed throughout cortical development as revealed by in situ hybridization (Allen Brain Atlas). (b) NeuroD2 protein (red) is expressed in the intermediate zone and cortical plate at E16.5, and in cortical layers L2 to L6 at P30 (c) and 1 year (d). (e) NeuroD2 protein (green) is co-expressed with Ctip2 (red) at P3 in L5. (f-g) At P30, NeuroD2 (red) never co-localizes with Gad67-GFP (green) in L5 and L6 (f), but co-localizes with Ctip2 in L5 (g).

Figure S2: Callosal size, cortical size and axon targeting identity of PN subsets.
(a-d) Callosal width was slightly decreased (a,b) but cortical width was unaltered (b,d) in *NeuroD2* KO mice. (e,f) Axonal targeting specificity of PN subtypes. Fluorescent retrograde cholera toxin beta injection in striatum, thalamus (e) and contralateral M1 L2-5 (f) led to unaltered distribution of retrogradely-labeled somata in ipsilateral motor/somatosensory cortex.

Figure S3: RNAseq experiments, Gene Ontology with ClueGO – complement to Figure 4. GO pie charts from ClueGO (Cytoscape).

Figure S4: Behavioral phenotypes in *NeuroD2* KO and HET mice- complement to Figure 4. (a,b) Time in the mouse chamber (M), center chamber (C) and empty cage chamber (E) during the 10 minutes social interaction (a) and social memory (b) tests. (c,d) Detailed behavior during 10 minutes intervals over the 1 hour open field assessment, including resting (c) and distance (d). (d) Time spent in the large center of the open field (red square in representative traces) was significantly increased in both HET and KO mice.

Figure S5: Schematic representation of 17q12 deletions in patients 3 and 4.